The Afterglow of the August 17$^{\text{th}}$ 2017 Binary Neutron Star Merger Multi-messenger Event

Raphaël Duque

Summary

Résumé

Contents

Part I
Introduction

1 MMT170817 – a historical event

Since August 17th 2017, a succession of astronomical observations have occured. These observations pertain to a new paradigm of astronomy, namely *multi-messenger astronomy*. Hence, we will refer to the collection of these observations as MMT170817, for *Multi-Messenger Transient 170817*.

MMT170817 is the outcome of an extraordinary instrumental effort provided by each of the fields of this multi-messenger astronomy. The detection of gravitational waves has ground-breakingly entered the astronomical landscape in September of 2015, as gravitational waves from all three phases (inspiral, merger, ring-down) of the coalescence of a binary black hole were detected in the *two* interferometers of the LIGO Scientific Collaboration. After a total of five such two-instrument detections, the gravitational interferometer network was augmented with the French-Italian Virgo instrument on August 1st 2017.

The first online gravitational wave detection of this *three*-instrument configuration occured on August 17th. This signal is associated with the inspiral phase of the merger of a binary neutron star. This joint detection allowed for the first-in-history astronomically significant gravitational wave triangulation of the source in the sky. This triangulation is given in terms both of sky-projected position and distance, drawing a three dimensional error box in the Universe. A prompt but meticulous optical search for a new electromagnetic source in this error box led to the first ever direct observation of a kilonova and the nuclear processes therein, and of a strongly atypically-behaved multi-wavelength afterglow, the observation of which carries on at the time of writing. The observations of these electromagnetic counterparts and the identificatoin of NGC4993 as the host galaxy of the event were done by a hitherto unseen joint effort from the astronomical community as a whole, mobilizing an impressive amount of ground-based instrumental resources.

With a slight delay with respect to the gravitational wave determined time of merger, the Fermi Gamma-ray Space Telescope and the INTEGRAL space observatory detected a weak short gamma ray burst, itself triangulated to a sky-position consistent with that indicated by the gravitational waves and the other electromagnetic counterparts.

The gravitational, gamma ray and other counterparts of this event are unambiguously associated, and thus are the multi-messenger manifestation of the first binary neutron star merger witnessed directly.

This work is a spark for the study of the merger of binary neutron stars. Focusing on the afterglow, we will through modelization attempt to a first understanding of this event and in particular of the outflow of matter produced by the merger and of the possible relativistic jet formed during the event.

2 Description of the multi-messenger observations

2.1 GW170817: gravitational waves from the inspiral phase

The inspiral phase gravitational waves (GW) were detected for the ~ 3000 last orbits of the binary[1]. This signal GW170817, reproduced figure 1, lasted ~ 100 s and ended at 12:41:04.4 UTC. It is the loudest gravitational wave signal detected yet, with a signal-to-noise ratio of 32.4. The GW signal infers masses in the range of $0.86 - 2.26$ $M_\odot$ (at 2σ). Given the ranges of measured galactic black hole masses, which are substantially higher than these, and the measured masses of some galactic binary neutron stars, which are consitent with these, a binary neutron star is the most likely nature of the GW progenitor. This is further supported by the detection of electromagnietic counterparts to this GW signal, indicating the presence of matter in the circum-merger environment after the merger, and thus the unlikelyness of a black hole in the initial binary.

The GW signal in the Virgo detector was low. This significantly constrained the localization of the source in the sky to a projected error box of 29 deg^2, and likely greatly decreased the duration of subsequent searches for electromagnetic counterparts.

---

[1]The information containd in this subsection and the following was synthesized from the multi-messenger detection publications [**?, ?, ?, ?**].

The GW signal luminosity distance to the source is 40^{+8}_{-14} Mpc, making of the GW and gamma ray bursts events the closest ever detected. This distance is further refined by combining GW data with EM observations of the host galaxy to 42.9 ± 3.2 Mpc. Similarly, the combination of the GW and EM data provides a viewing angle (from our light-of-sight to the angular momentum of the binary) constrained to being less than 28 deg.

An essential feature of GW170817 is the non-detection of a postmerger ring-down signal, i.e. the signal from the gravitational radiation emitted by the relaxation of the merger product to its final state of equilibrium. This non-detection signifies either that the corresponding radiation was not emitted, which would likely be the case in the remnant object being a neutron star, or that the signal was to weak to be picked up. Moreover, had the final object been a black hole, its ring-down signal would have peaked at frequencies well out of the detectors' sensitive bands, given the masses at hand. In any event, the nature of the final object is undetermined by the GW signal.
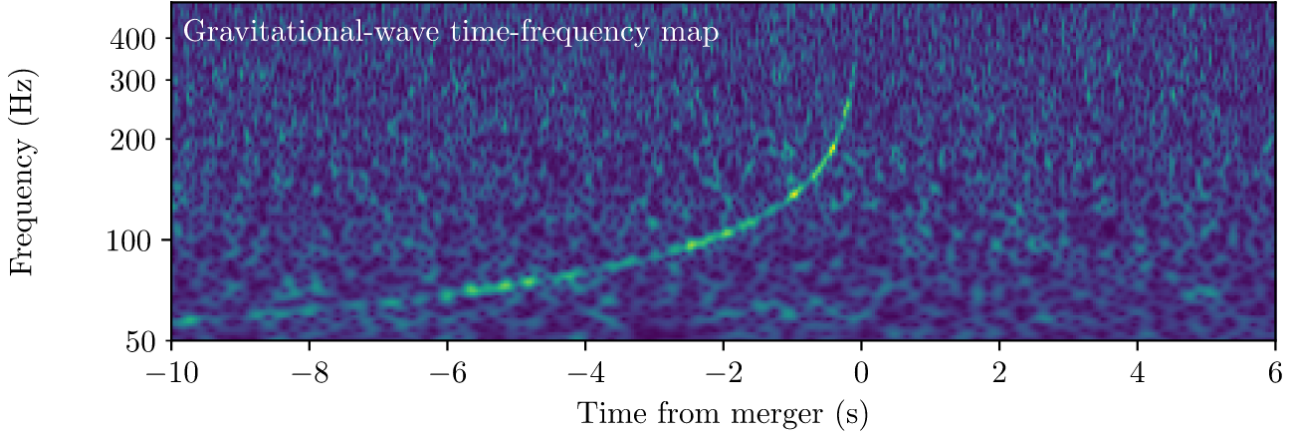

Figure 1: Spectrogram of a combination of both LIGO interferometers' data from GW170817 ([**?**]). Note the non-detection of a ring-down signal. The peak luminosity of the GW event is $\sim 9\ M_\odot c^2/$s ([**?**]).

2.2 GRB170817A: the gamma-ray burst

The gamma ray burst (GRB) event started 1.72 s after the GW data merger time. Its duration was 2.0 s, placing it in the short GRB class with a confidence level of $\sim 72\%$. GRB170817A's total isotropic-equivalent radiated energy was $\sim 10^{47}$ erg, around 4 orders of magnitude weaker that typical short gamma ray bursts, though photons with energies as high as 185 keV were emitted.

Moreover, it appears that the light curve of GRB170817A presents two distinct components, one lasting 0.58 s, and a later second lasting 1.1 s. Spectrally, the first component resembles a typical non-thermal short GRB emission, and the second on the other hand is best fit by a thermal emission of temperature $\sim 10^7$ K.

Furthermore, as illustrated in figure 2, GRB170817A is an outlier of the E_p-$L_{\rm iso}$ relation, also know as the Yonetoku relation ([**?**]). In this relation which is broadly respected by short GRBs, E_p and $L_{\rm iso}$ are the peak photon energy and isotropic equivalent luminosity of the burst at its peak, and they are positively correlated. Even when correcting for the possibly non-zero viewing angle, and placing the burst as seen closer to its axis, GRB170817A remains an outlier of the Yonetoku relation.
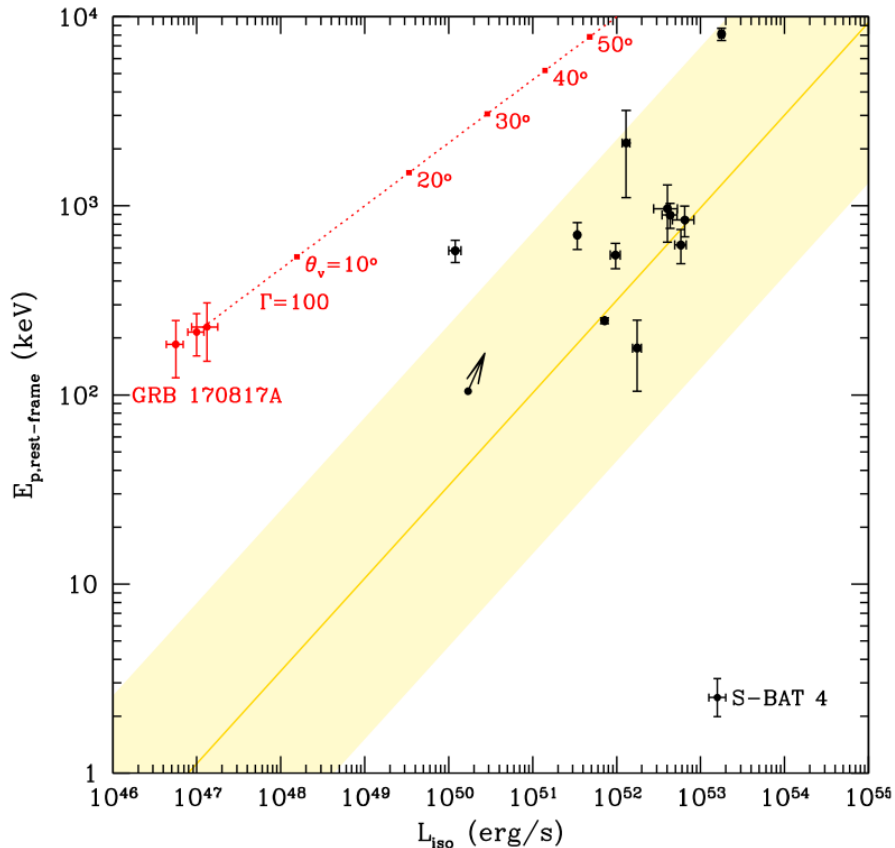
Figure 2: The Yonetoku relation for the Swift BAT 4 catalog bursts (black crosses, [**?**]) and GRB170817A. The values of E_p and L_{iso} that would have likely been measured for other viewing angles form a line in this diagram.

All of these observations indicate the *atypical* character of GRB170817A and of MMT170817 as a whole. More precisely, these remarks lead to interrogations on the emission processes responsible for GRB170817A. Standard understanding of GRBs imply relativistic jets and energy dissipation into gamma radiation therein. Are GRBs from neutron star mergers comprehensible in such standard models? Are they a particular case of these models? Or do they require a specific modelling?

Other weak short GRBs have been observed in the past. An example is GRB980425 which stood out as an atypical event among short GRBs for its low luminosity. It was then found ([**?**]) that the internal shock model allowed such events, provided the outflow be slower and less energetic.

2.3   AT 2017gfo: the kilonova

The optical counterpart AT 2017gfo (IAU designation) was discovered ~ 11 h after the merger event. It was located in the lenticular galaxyNGC4993 within the ESO 508 group of galaxies in Hydra. Upon discovery, the r band magnitude was measured to ~ 17, equivalent to an absolute magnitude of –16.

In the following days, until dimming to non-detection limits of AT 2017gfo, spectra of the transient were measured. The time evolution of these spectra is illustrated figure 3. These are associated with thermal radiation of an optically thick mass of dynamical (or tidal) ejecta from the merger event. It is understood that the neutron-rich matter ejected by the merger event is the site of r-process nucleosynthesis, that is the synthesis of extremely heavy nuclei by rapid neutron capture in a neutron-dense environment, and the subsequent decay of these nuclei to heavy elements such as the lanthanides and actinides. The decay of the nuclei are a heat source within the kilonova, and the extremely opaque medium composed of heavy nuclei insures its thermalization. Finally, the sudden decompresion of this once-neutron-star material into the rarified external medium drives the rapid expansion of3 the ejecta.

This vision is further supported by the claim to the detection of atomic cesium and tellurium ($Z = 55$ and 52)absorption lines in the transient's spectrum [**?**].
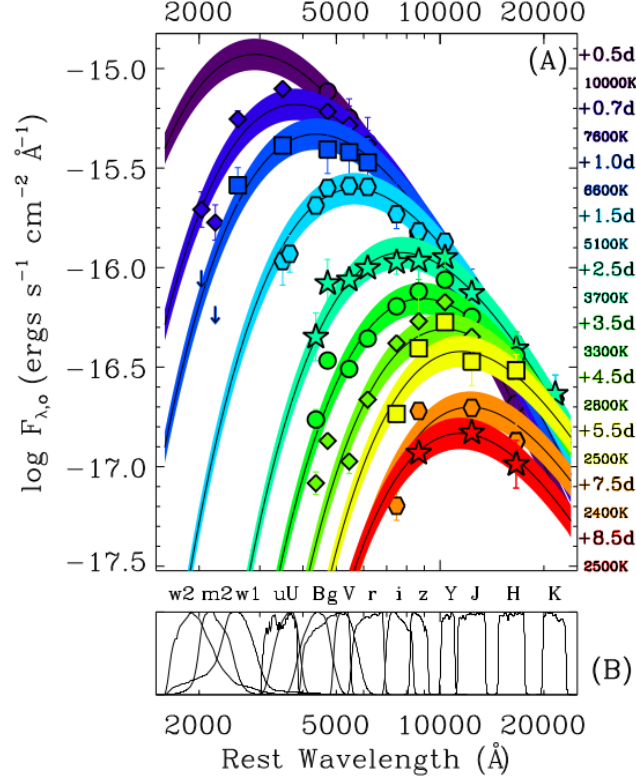
Figure 3: Time evolution of the spectrum of AT 2017gfo ([**?**]).

2.4 The afterglow signal

Counterparts in the X-ray and radio bands were detected to significant levels 9 days and 15 days post-merger. When the kilonova signal had sufficiently decayed at 150 days post-merger, an optical band afterglow was detected as emerging from the dimming kilonova signal.

The afterglow photometry points in these bands until ~ 250 d post-merger are reported figure 4. An essential feature of these afterglow light curves are their homothetic structure, i.e. their seems to exist a time-independent index k such that for two frequencies ν and ν', we have $F_\nu = \left(\frac{\nu}{\nu'}\right)^k F_{\nu'}$.

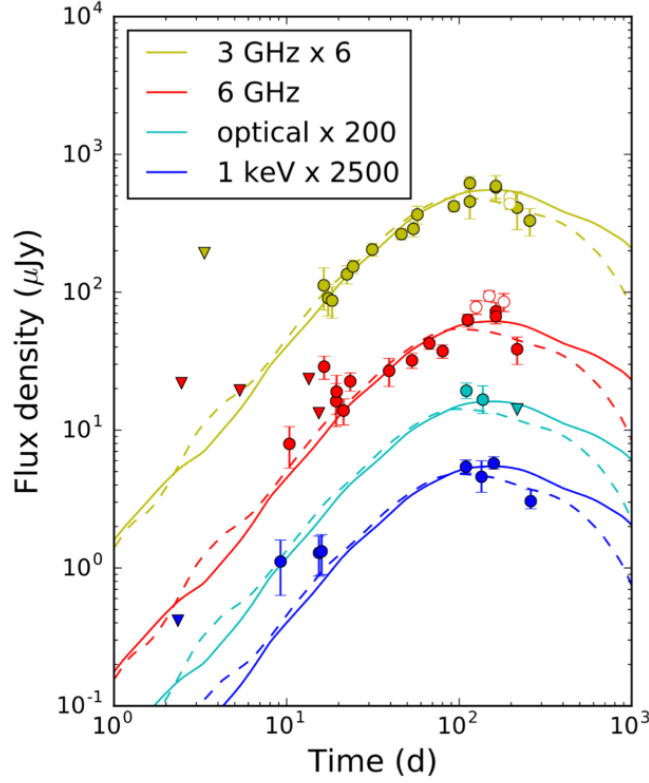Figure 4: Afterglow photometry points in various bands ([**?**]). Notice the homothetical structure of the flux from band to band.

As we will shortly see, this structure is a first indication of which radiation process is at play in the afterglow, and subsequently allows to reduce the number of light curves considered for our study to a single one.

Another important feature of this afterglow emission is that it is long-lived. Indeed, the radio flux increased steadily until ~ 160 d post-merger, then commenced a steady decrease and it still observed at the time of writing. A comparison of the afterglow of MMT170817 with some of the most long-lived short GRB afterglows from the total Swift catalog is shown in figure 5. It is evident that MMT170817 is pecliar with respect of all of these.
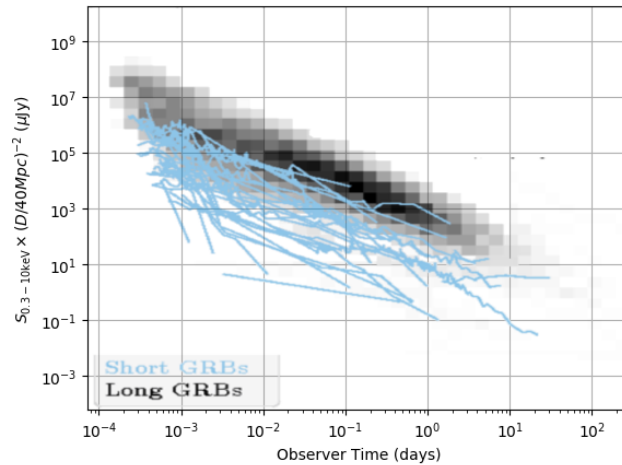

Figure 5: Some of the most long-lived afterglows from the Swift catalog (doted lines, X-ray data), and the afterglow from MMT170817.

3 Goal of this work: the afterglow of MMT170817 as an insight on the merger event

The merger of a binary neutron star is a complex phenomena. It most likely implies various physical components (compact objects, jets, ejectas, winds) which are subject to many dynamical and radiative processes (shock formation, nuclear processes, synchrotron emission, etc.). A coherent description of the binary neutron star merger phenomena, from the inspiral phase to the electromagnetic afterglow, is still to be found. Most likely, the combination of all the multi-messenger observations from a large number of events will be necessary to obtain this accurate description, as each signal bares the signature of the state of the phenomenon at different times.

In particular, the afterglow holds information on the state of matters at late times, and is a first step one may take to approach the event in its entirety. The goal of this work is precisely to study the afterglow of MMT170817 in the perspective of later inferring information on the earlier phases of the event: the nature and formation of the resulting compact object, the origin of the gamma ray burst, the dynamical properties of the outflow, the development of the kilonova, etc.

The questions this work adresses are thus the following:

1. What is the geometry and the structure of the outflow of matter responsible for the afterglow?

2. What are the characteristics of the circum-merger medium which this outflow penetrates?

3. By which means is the kinetic energy dissipated into the afterglow radiation?

4. Was a relativistic jet produced in the merger event?

5. By which angle do we currently see the system?

6. Which afterglow signals would we have seen, had we seen the event from a different viewing angles?

Part II
Modelling the afterglow of MMT170817

Note on the physical origin of the afterglow. As insisted upon in the introduction, MMT170817 is an *atypical* event. Nonetheless, the numerous observations of remnants and afterglows of transient electromagnetic events (such as supernovae and gamma ray bursts) indicate a common explanation of afterglows having timescales from days to years, such as that of MMT170817. Matter which is ejected during the previous phases of the phenomenon travels in the local external medium faster than the speed of sound. A shock thus forms at the interface of this shock with the interstellar medium. Interstellar material accumulates at this shock front, is excited and radiates. As the material accumulates, the shock decelerates. The exact nature and origin of the ejected matter, and the characteristics of the medium in which it evolves depends on the specific astrophysical phenomena at hand.

Thus, the models which we will describe here and later confront to observations will concern the radiation of interstellar material which is shocked and radiates through the synchrotron process at the front of a shock formed by the piston effect of ejecta from the merger on the exterior medium, while this shock decelerates as it penetrates the ISM.

Figure 6: Cut across the shock front, showing the ejected matter, and the interstellar material accumulating a the shock front.

4 The physics of afterglows: deceleration dynamics, radiation and astronomical observables

In this section, we will review the physics which will take part in the modelling of the afterglow of MMT170817. We will successively describe the deceleration of the remnant expanding in the interstellar medium, the radiation of matter at the shock front, and derive the electromagnetic signals which arise from this radiation. The more technical details of these physical processes may be found in *Appendix B.*

4.1 Relativistic deceleration

We now describe the dynamics of the deceleration of the remnant in the ISM. We will consider for this work two different structures for the ejected matter: a *mono-kinetic ejecta*, or a *radially stratified ejection.*

We will follow the Lorentz factor $\Gamma(r)$ of the ejected matter once it has reached the exterior radial coordinate r.

Mono-kinetic ejection. In this case, the matter is ejected with initial energy E_0 and a single Lorentz factor Γ_0. By plowing through the ISM, the shock sweeps up interstellar material and decelerates. By denoting $M_{\rm ej}$ the mass of the ejected matter, $m(r)$ the accumulated mass swept up by the shock at radius r from the point of ejection, conservation of energy implies that the initial total energy $\Gamma_0 M_{\rm ej} c^2 + m(r)c^2$ is distributed in the ejected mass energy $\Gamma(r) M_{\rm ej} c^2$ and the internal energy of the swept up mass $\Gamma(r)^2 m(r) c^2$. Thus:

$$\Gamma(r)^2 m(r) + \Gamma(r) M_{\rm ej} = \Gamma_0 M_{\rm ej} + m(r)$$

Details on the $\Gamma^2 mc^2$ form for the thermal energy of the swept-up mass can be found in *Appendix B.*

We will consider for our purposes a homogeneous medium with numeric density n.

Suppose that the mass $M_{\rm ej}$ was ejected into a solid angle Ω by the central source, for instance in the form of a cone. Then if we neglect any lateral expansion of the ejected matter, the swept us mass at radius will be[2]:

$$m(r) \;=\; \Omega \int_0^r dr' r'^2 n m_P$$

Thus by introducing the isotropic-equivalent ejected mass $M_{\rm iso} = 4\pi M_{\rm ej}/\Omega$, the dimensionless mass parameter $\mu(r) \equiv \frac{m(r)}{M_{\rm iso}/\Gamma_0}$, writes:

$$
\begin{aligned}
\mu(r) \;&=\; \frac{\Omega \int_0^r dr' r'^2 n m_P}{M_{\rm ej}/\Gamma_0} \\
&=\; \frac{4\pi r^3}{3 M_{\rm iso}/\Gamma_0} n m_P
\end{aligned}
$$

which no longer depends on the solid angle of ejection.

We may identify the *deceleration radius*, $R_{\rm dec} = \left(\frac{3 E_0}{4\pi n m_P \Gamma_0^2 c^2} \right)^{1/3}$, such that:

$$\mu(r) = \left(\frac{r}{R_{\rm dec}} \right)^3$$

And finally, the solution for $\Gamma(r)$ is easily found to be:

$$\Gamma(r) = \Gamma_0 \frac{-1 + \sqrt{1 + 4\mu(r) + \frac{4\mu(r)^2}{\Gamma_0^2}}}{2\mu(r)}$$

Phases of deceleration. We observe three phases in the deceleration of the shock front:

1. For $\mu(r) \ll 1/4$, i.e. $r \ll R_{\rm dec}$, in the *coasting phase*, no deceleration occurs:

$$\Gamma(r) \simeq \Gamma_0$$

2. For $1/4 \ll \mu(r) \ll \Gamma_0^2$, i.e. $R_{\rm dec} \ll r \ll \Gamma_0^{2/3} R_{\rm dec} \equiv R_{\rm N}$ (*newtonian radius*), the front is in a *relativistic deceleration phase*, during which the swept-up mass progressively reaches $\Gamma_0 M$:

$$\Gamma(r) \simeq \frac{\Gamma_0}{\sqrt{\mu(r)}} = \Gamma_0 \left(\frac{r}{R_{\rm dec}} \right)^{-3/2}$$

3. For $\Gamma_0^2 \ll \mu(r)$, i.e. $R_{\rm N} \ll r$:

$$\Gamma(r) \simeq 1$$

and

---

[2] In all generality, we should consider the average mass per particle in the local exterior environment instead of m_P.

$$\check{(}r) \simeq c\sqrt{1 - \frac{1}{\Gamma_0}} \left(\frac{r}{R_\mathrm{N}}\right)^{-3/2}$$

This is the *Newtonian phase*, and we see that deceleration to non-relativistic velocities requires the sweeping up of a mass on the order of $\Gamma_0 M$.

Radially stratified structure. In this case, we suppose that the matter was ejected with an inhomogeneous distribution of velocities: some components were ejected with larger energies than others. We parametrize this distribution giving a cumulative ditribution $E(> \Gamma)$ of energies. It is such that at ejection, the total energy of the matter having a Lorentz factor larger than a given $\hat{\Gamma}$ is $E(> \hat{\Gamma})$.

After the ejection, the higher-velocity component of the ejecta will form the shock front, while the rest of the ejecta lags behind. The front shock decelerating in the ISM, the slower components will catch up to the front shock. This way, the catching-up matter will slow the deceleration down, until the slowest component has caught up. Then, the dynamics are the same as a mono-kinetic ejection starting from the slowest initial velocity.

How to write energy conservation in this case? If the front shock has reached a Lorentz factor Γ (at r), it means that all the energy which was initially available to the ejected matter with Lorentz factors above Γ has already caught-up and been injected into the shock, since we neglect the time it takes for matter to catch-up to the shock. But the energy injected by the shock is that held in internal energy form by the swept-up material at the shock, as in the mono-kinetic ejection case. Thus, we have:

$$\Gamma(r)^2 m(r)c^2 = E(> \Gamma(r)) + m(r)c^2$$

Notice that this is an implicit equation on $\Gamma(r)$, and that we do not consider here an initial bulk mass which would have a initial energy of $\Gamma_0 M c^2$. Considering an additional bulk mass in this process would simply amount to a discontinueous function $E(> \Gamma)$.

In the case of a homogeneous medium, this reduces to:

$$\frac{4\pi}{3} r^3 n m_P c^2 (\Gamma(r)^2 - 1) = E(> \Gamma)$$

Alternatively, we parametrize the distribution in terms of the *relativistic 4-velocity $u = \Gamma\beta$*.

It follows that if the total initial energy is E_0 and the largest (resp. smallest) velocity in the ejecta is u_M (resp. u_m), then the energy distribution function can be written as:

$$E(> u) = E_0 g(u)$$

,

where g is a function equal to 1 for $u < u_m$, to 0 for $u_M < u$, and decreases between u_m and u_M.

The simplest functional form for g which meets these requirements is a power-law with some positive index α containing all the unknown physics of the ejection event. Explicitly, the final deceleration dynamics equation is (note that $\Gamma^2 - 1 = (\Gamma\beta)^2$):

$$\frac{4\pi r^3 n m_P c^2 u(r)^2}{3 E_0} = \frac{u(r)^{-\alpha} - u_M^{-\alpha}}{u_m^{-\alpha} - u_M^{-\alpha}}$$

In this case, solving for $\Gamma(r)$ (or equivalently $u(r)$) is not analytical, and we will find $\Gamma(r)$ with help of numerical integration. For our purposes, we fix the value of α to the fiducial value of 5 ([**?**]).

4.2 Synchrotron radiation and self-absorption

We now turn to the radiation emerging from the shocked matter, which constitutes the afterglow emission. From now on, we will denote with primes $'$ the value of quantities measured in the frame of the expanding matter, and without primes those measured in the laboratory (exterior) frame.

Shock conditions on numeric density and specific internal energy. What are the conditions at the shock front, where interstellar material is excited and radiates? They are given by the Rankine Hugoniot (e.g [**?**]) relations. In the case of ultrarelativistic matter (with an adiabatic index of $\gamma = 4/3$), the shock-frame numeric density and internal-to-mass energy ratio are:

$$n' = (4\Gamma + 3)n$$

and

$$\epsilon' = (\Gamma - 1)$$

Electron population and magnetic field. The physical process we consider for radiation is synchrotron radiation. The energy deposited by the shock contributes to the two factors of synchrotron radiation: a magnetic field and a population of relativistic electrons.

The microphysics of the emergence of magnetic fields in astrophysical shocks are unclear (nonetheless, see *Appendix E* for a short discussion). From our standpoint, we are concerned only with the strength of the field, and will consider that a free microphysical parameter ϵ_B relates the field magnitude to the shock-frame energy density, such that:

$$\frac{B'^2}{8\pi} = \epsilon_B n' \epsilon' m_P c^2$$

Likewise, we will consider that the electron population has a simple energy spectrum: it is a power law of index p in the Lorentz factor space as of some minimal Lorentz factor Γ_m. Note that the energy contained in the electron population is *not directional*. On the contrary to the exterior kinetic energy of the shock (emcompassed in $\Gamma(r)$), this electron energy distribution arises from an isotropic momentum distribution in the local frame, and thus may be regarded as internal energy.

We introduce yet another microphysical parameter ϵ_e, which relates the proportion of the local internal energy distribution which is carried by the electrons. By requiring that the electrons carry a fraction ϵ_e of the total internal energy, we write:

$$\int_{\gamma_m}^{\infty} d\gamma \mathcal{N}(\gamma) \gamma m_e c^2 = \epsilon_e \epsilon' m_P c^2$$

Also, normalization of the population density writes:

$$\int_{\gamma_m}^{\infty} d\gamma \mathcal{N}(\gamma) = 1$$

With an energy density $\mathcal{N}(\gamma) \propto \gamma^{-p}$, one obtains:

$$\gamma_m = \epsilon_e \frac{m_P}{m_e} \frac{p-2}{p-1} (\Gamma - 1)$$

and finally we have:

$$\mathcal{N}(\gamma) = \begin{cases} 0 & \text{for } \gamma < \gamma_m \\ \frac{p-1}{\gamma_m} \left(\frac{\gamma}{\gamma_m} \right)^{-p} & \text{for } \gamma_m < \gamma \end{cases} \tag{1}$$

The synchrotron spectrum of a power-law population of electrons. It can be shown (see e.g. [?], sec. 6) that the source-frame synchrotron spectral power emitted by a single electron of Lorentz factor γ_e in a magnetic field B varies as $\nu'^{1/3}$ until a maximum frequency:

$$\nu'_s(\gamma_e) = \gamma_e^2 \frac{eB}{2\pi m_e c} \tag{2}$$

and then decreases exponentially. The maximum spectral power is:

$$P'_{\max} = \frac{m_e c^2 \sigma_T}{3e} B \tag{3}$$

where σ_T is Thomson cross-section.

It follows that the total power emitted by the electron is approximately

$$P' \sim \int_0^{\nu'_s(\gamma_e)} d\nu' P'_{\max} \left(\frac{\nu'}{\nu'_s(\gamma_e)} \right)^{1/3} \tag{4}$$

$$\sim P_{\max} \nu'_s(\gamma_e) \tag{5}$$

13

Thus the time scale for energy loss by synchrotron radiation is:

$$t'_r = \frac{\gamma_e m_c c^2}{P'} \tag{6}$$

$$= \frac{6\pi m_e c}{\sigma_T \gamma_e B^2} \tag{7}$$

How does this compare to the time scale for adiabatic cooling due to the expansion of the shell?

The exterior frame expansion time scale (the *dynamical* time-scale) is $t_d = \frac{v}{R}$, needed for the remnant to double its radius. In the shock-frame this is $t'_d = \frac{v}{\Gamma R}$.

We denote by γ_c the Lorentz factor of an electron which cools by synchrotron radiation in a dynamical time-scale, i.e. $t'_r = t'_d$. In other words:

$$\gamma_c = \frac{6\pi m_e c}{\sigma_T B^2 t'_d}$$

Furthermore, we introduce the synchrotron characteristic frequencies of the electron population ν'_m and ν'_c as the frequency of peak emission from electrons with Lorentz factors γ_m and γ_c:

$$\nu'_c = \nu'_s(\gamma_c) \tag{8}$$

$$\nu'_m = \nu'_s(\gamma_m) \tag{9}$$

For an electron of Lorentz factor $\gamma_e > \gamma_c$, the total energy goes as $E \propto \gamma_e$, whereas the radiated power is as $P' \propto \gamma_e^2$. Thus as the electron cools from γ_e to γ_c, the bulk of the radiation is emitted on the $[\nu'_c, \nu'_e]$ portion of the spectrum, where the spectral power is $\propto \nu'^{-1/2}$.

The overall power spectrum for a single electron is thus composed of three segments: a power law as $\nu'^{1/3}$ for $\nu' < \nu'_c$, a power law as $\nu'^{-1/2}$ for $\nu'_c < \nu' < \nu'_s(\gamma_e)$, and an exponential cut-off for larger frequencies. The maximum spectral power is P'_{max}, attained at ν'_c.

Coming back to the entire population of the electrons in the shock, we determine the total emission spectrum by integrating on the Lorentz factor distribution $\mathcal{N}$ as in eq. 1. For this, two cases can arise:

1. $\gamma_m < \gamma_c$, which we call *slow cooling*, because the bulk of the population has $\gamma_e < \gamma_c$ and thus cools on time-scales larger than the dynamical t'_d, thus slower than the adiabatic cooling process. In this case, the average power spectrum per electron is:

$$P' = P'_{max} \times \begin{cases} (\nu/\nu_m)^{1/3} & \text{for } \nu < \nu_m \\ (\nu/\nu_m)^{-(p-1)/2} & \text{for } \nu_m < \nu < \nu_c \\ (\nu_c/\nu_m)^{-(p-1)/2}(\nu/\nu_c)^{-p/2} & \text{for } \nu_c < \nu \end{cases} \tag{10}$$

2. $\gamma_c < \gamma_m$, the state of *fast cooling*, because then all of the electrons cool in a time-scale smaller that the dynamical time-scale. Then, the average power spectrum per electron is:

$$P' = P'_{max} \times \begin{cases} (\nu/\nu_c)^{1/3} & \text{for } \nu < \nu_c \\ (\nu/\nu_c)^{-1/2} & \text{for } \nu_c < \nu < \nu_m \\ (\nu_m/\nu_c)^{-1/2}(\nu/\nu_m)^{-p/2} & \text{for } \nu_m < \nu \end{cases} \tag{11}$$

Synchrotron absorption and inverse-Compton diffusion. In addition,

4.3 Derivation of the astronomical observable: flux density

Given a rest-frame emission spectrum for the matter in the exanding shock and a velocity of the shock, what flux will a distant observer measure? Suppose that at exterior time $t = 0$, the matter is ejected, and that the shell has reached a radius of R and Lorentz factor Γ by time t. Suppose a chunk of matter in the shock front emits some light with frequency ν' in its rest frame. We must discuss the arrival time and frequency of the light to the observer.

Figure 7: The geometry of the remnant. A spherical shell-like shock front (or a part of a sphere) is expanding at speed $\beta(t)$, while every particle radiates in its own reference frame according to an emissivity j'.

Simple discussion: matter moving towards the observer. Suppose that the emitter is moving towards the observer, like the red dot in figure 7. Then the observed frequency at the time of arrival of the emitted light will simply be $\nu = \frac{\nu'}{\Gamma(1-\beta)}$ by relativistic Doppler shifting[3]. Γ and β here must be considered at the time of emission t of the light of course.

Let t_{obs} denote the time of arrival to the distant observer of the light emitted at t. After emission, the light travels the distance $D - R$ before arrival. Thus, $t_{\mathrm{obs}} = t + \frac{D-R}{c}$. D/c here is nothing else than the 120 Myr the first emitted light took to reach us. If we count time from the source-frame beginning of the event, we can drop this delay, and thus write:

$$t_{\mathrm{obs}} = t - R/c \tag{12}$$

Let us introduce the shock-frame time coordinate t', such that $dt' = dt/\Gamma(t)$ and $t' = 0$ at ejection.

What flux will be received from this chunk of emitting matter? We introduce the rest-frame emissivity j' of the matter (in units of erg/s/cm^3/Hz $= 10^{23}$ Jy). The power emitted isotropically in all rest-frame directions at shock-frame time t' by a volume dV' of this matter in the rest-frame frequency interval $d\nu'$ around ν' is $j'(\nu', t')dV'd\nu'$. Through Lorentz transformations, it can be shown that j/ν^2 is conserved (see e.g. [**?**], sec. 4).

It thus follows that the received spectral flux density (in units of ergs/s/cm^2/Hz) at observer time t_{obs} and frequency ν will be:

$$dF(\nu, t_{\mathrm{obs}}) = \frac{1}{4\pi D^2} \frac{j'(\nu\Gamma(t)(1-\beta(t)), t')}{(\Gamma(t)(1-\beta(t)))^2} dV$$

where t and t' are simply the source-frame and shock-frame time coordinates of the event of the emission ofthe light which was received at observer time t_{obs}. Of course, since the dynamics of the shell are followed according to t, we will express j' as a function of t later.

General discussion: flux from an extended remnant. Let us now consider a chunk of matter moving with an angle θ with respect to the line of sight (like the red dot on figure 7). Then the Doppler shifting reads more generally $\nu = \frac{\nu'}{\Gamma(1-\beta\cos\theta)}$, and the distance to travel for the light from emission to reception is $D - R\cos\theta$, thus the time of arrival is:

$$t_{\mathrm{obs}} = t - R\cos\theta/c$$

(13)

Notice that in this case, for a same arrival time, the time of emission is dependent on θ in such a way that at one given instant, the observer is receiving light emitted by the shell at earlier times (and thus different β and j') for larger angles from the line of sight.

Thus, by neglecting absorption and diffusion of radiation from the remnant by other parts of the remnant on the line of sight, we write the total flux measured at time T as:

$$F(\nu, T) = \frac{1}{4\pi D^2} \int_0^\infty dt \int_0^\infty dr \int \int_{\Omega_E} d\theta d\phi r^2 \sin\theta \mathcal{D}(\theta, t)^2 \left[j'\left(\frac{\nu}{\mathcal{D}(\theta, t)}, r, t\right) \delta\left(T - t + \frac{r\cos\theta}{c}\right) \right] \tag{14}$$

where $\mathcal{D}(\theta, t) = \frac{1}{\Gamma(t)(1-\beta(t)\cos\theta)}$ is the time and angle-dependent Doppler factor of the matter of which the radiation will be received at T, and Ω_E is the total solid angle occupied by the remnant. This equation takes into account the delay on light arrival time (through the δ function), the Doppler

---

[3]There are many conventions for the expression of the Doppler factor and the sign of β. Noticing that $\Gamma(1+\beta) = \frac{1}{\Gamma(1-\beta)}$, we might have as well written $\nu = \Gamma(1+\beta)\nu'$.

frequency shifting (through the evaluation of j' at $\nu/\mathcal{D}$) and the relativistic beaming of radiation (through the integration of $j'/\mathcal{D}$).

For a spherical remnant, Ω_E is the entire sphere. For a jet, Ω_E is a portion of the sphere of subtending half-angle usually denoted θ_j (as well as the diametrally-opposite portion of the sphere if we include the counter-jet).

Figure 8: Geometrical configurations for fluxes from *(a)* a spherical remnant, *(b)* a jet seen on axis, *(c)* a jet seen off axis.

Flux from a jet seen on axis. Thus, for given dynamics $\Gamma(t)$ and emissivity j', the flux received from different geometries will differ according to the integration domain for θ and ϕ. Suppose that the flux from a sphere is given as $F^{\mathrm{iso}}(\nu, T)$ (as in figure 8, *a*), can we easily deduce the flux from a jet seen through its axis (as in figure 8 *b*)?

At early times, the radiation from matter on the side of the sphericl remnant will not be observed, because it will be beaming-suppressed if Γ is too large. Thus, the radiation will be the same as that from a jet, where hte radiation from matter on the side is not observed simply because there is no matter on the side.

At later times, when the remnant has decelerated, the emission from side matter will start to be observed in the spherical case, but still not in the jet case. Thus, it is only at late times that an observer which is observing a jet will realize that the remnant is jetted, because the emission from the side will be *missing*.

How may we quantify this change in observed radiation? For a jet, the matter emitting the radition is contained in a solid angle $\Omega_j = 4\pi(1 - \cos\theta_j)$. In both the spherical and jet cases, the radiation from the matter is beamed into a solid angle of half-angle $1/\Gamma$: $\Omega_b = 4\pi(1 - \cos(1/\Gamma))$. In consequence, the flux from the two cases will be equal while the matter outside of Ω_j is too beamed to be observed, i.e. $\Omega_b \ll \Omega_j$. Conversely, after some deceleration, the jet observer will observe less radiation because its beaming solid angle exceeds the jet solid angle, i.e. when $\Omega_j \ll \Omega_b$. When this moment – the *jet break* – has occured, then the jet observer will observe only a portion Ω_j/Ω_b of the radiation seen be a spherical remnant observer, because the radiation which is no longer beamed to the observer cannot be replaced by radiation of matter on the side.

Developing for $\Gamma \gg 1$ and $\theta_j \ll 1$ leads to $\Omega_b \simeq \pi/\Gamma^2$ and $\Omega_j \simeq \pi\theta_j^2$. Thus the flux $F^{\mathrm{on}}(\nu, T, \theta_j)$ seen by an observer in the axis of a jet of half-aperture θ_j can be expressed in terms of the flux observed from a spherical remnant with the same dynamics and emission as:

$$F^{\mathrm{on}}(\nu, T, \theta_j) = \begin{cases} 1 & \times & F^{\mathrm{iso}}(\nu, T) & \text{if } \Gamma\theta_j \gg 1 \\ (\Gamma\theta_j)^2 & \times & F^{\mathrm{iso}}(\nu, T) & \text{if } \Gamma\theta_j \ll 1 \end{cases}$$

(15)

Flux from a jet seen off axis. We now turn to the radiation observed from a jet seen with an angle θ_{obs} from it axis (as in figure 8 *c*). We suppose that $\theta_{\mathrm{obs}} \gg \theta_j$. Then, we can neglect the variation of the global viewing angle (which is in $[\theta_{\mathrm{obs}} - \theta_j, \theta_{\mathrm{obs}} + \theta_j]$) and consider that the the emission from the cone will be frequency-shifted, delayed and suppressed by beaming as a whole, as if seen from an angle of θ_{obs}.

We thus consider the flux from a jet on axis F^{on} and apply a transformation to delay,frequency-shift, and beam the emission alltogether. The arrival time will be $t - R\cos\theta_{\mathrm{obs}}/c$ and no longer $t - R/c$, and the frequency in a factor of $\Gamma(1 - \beta\cos\theta_{\mathrm{obs}})$ of the emitted frequency and no longer of $\Gamma(1 - \beta)$.

Similarly, the spectral luminosity varies as $\mathcal{D}^3$, thus we write:

$$F^{\mathrm{off}}(\nu, T, \theta_j, \theta_{\mathrm{obs}}) = a^3 F^{\mathrm{on}}\left(\frac{\nu}{a}, bT, \theta_j\right)$$

(16)

with:

$$a = \frac{1 - \beta}{1 - \beta \cos \theta_{\mathrm{obs}}}$$

and

$$b = \frac{1 - \frac{R}{ct}}{1 - \frac{R \cos \theta_{\mathrm{obs}}}{ct}}$$

Simplification of the spherical remnant flux in our case of synchrotron emission. In our case, we will not calculate the flux by integrating j' as in eq. 14. We will instead greatly simplify the calculation, and consider the remnant as radiating altogether according to the spectrum of eq. **??**, and apply a uniform factor Γ to account for Doppler frequency shifting. What's more, we will not integrate on equal-arrival times, but consider that the remnant emits entirely synchronousely. Thus, we will calculate the arrival time as $t_{\mathrm{obs}} = t - R/c$.

In the case of a jet, we will apply the corrections of eq. 4.3 and 16 for on-axis and off-axis observations.

In practice, this amounts to the following flux:

$$F^{\mathrm{iso}}(\nu, T) = \frac{N_e}{4\pi D^2} P_{\max} \times \begin{cases} (\nu/\nu_c)^{1/3} & \text{for} \quad \nu \ll \nu_c \\ (\nu/\nu_c)^{-1/2} & \text{for} \quad \nu_c \ll \nu \ll \nu_m \quad \text{for} \quad \nu_c \ll \nu_m \quad \text{fast cooling} \\ (\nu_m/\nu_c)^{-1/2}(\nu/\nu_m)^{-p/2} & \text{for} \quad \nu_m \ll \nu \end{cases} \tag{17}$$

$$= \frac{N_e}{4\pi D^2} P_{\max} \times \begin{cases} (\nu/\nu_m)^{1/3} & \text{for} \quad \nu \ll \nu_m \\ (\nu/\nu_m)^{-(p-1)/2} & \text{for} \quad \nu_m \ll \nu \ll \nu_c \quad \text{for} \quad \nu_m \ll \nu_c \quad \text{slow cooling} \\ (\nu_c/\nu_m)^{-(p-1)/2}(\nu/\nu_c)^{-p/2} & \text{for} \quad \nu_c \ll \nu \end{cases} \tag{18}$$

where $N_e = 4\pi R^3 n/3$ is the number of electrons in the shock, $P_{\max}$ is the Doppler shifted (simply by Γ as our simplification states) synchrotron spectrum peak flux, as in eq. 3, and the characteristic frequencies are given in eq. 8 and also Doppler shifted. Time is numerically integrated from the conditions $R = 0$ at $T = 0$, and $dT = dt - \frac{dR}{c}$ as in eq. 12, equivalent to $dT = \left(\frac{1}{\beta} - 1\right)\frac{dR}{c}$.

Final parametrization. In conclusion, the overall parameters necessary to predict afterglow light curves are:

- For the external medium: n and ϵ_B,

- For a quasi-spherical remnant: E_0 and Γ_0 in the case of a mono-kinetic ejection, or E_0, u_m and u_M in the case of a structured ejecta,

- For a jetted ejecta: additional geometrical parameters θ_j and θ_{obs} with respect to a quasi-spherical remnant.

4.4 An illustration of some predicted light curves

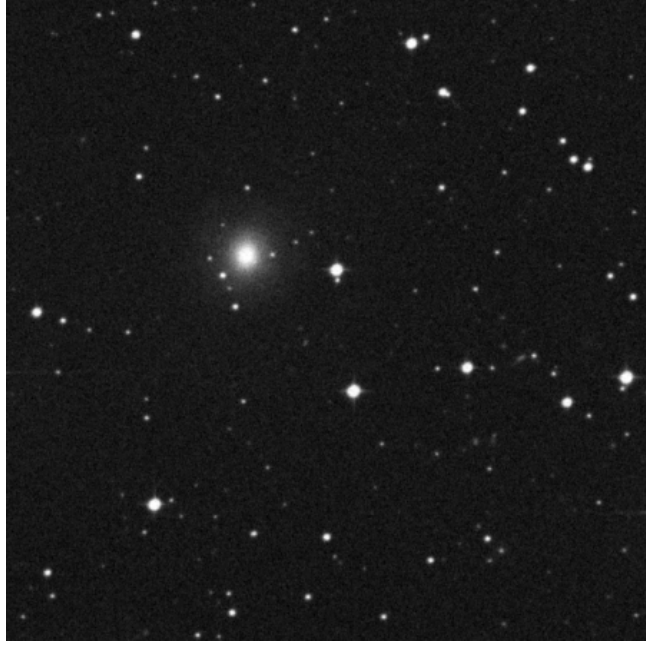To conclude this section, we will illustrate the models with some predicted light curves.

Figure 9: Some light curves as calculated by our model.

Why does a light curve peak? dynamical or spectral regime shifts.

On the validity of the simplifications used in our study In order to evaluate the errors commited on the light curves produced by our simplified calculations (for spherical models as well as jets), some light curves on typical ranges of parameters are compared with those produced by full-fledged simulations, which do perform equal arrival time intergration in general conic geometries. Figure 10 reports such comparisons.
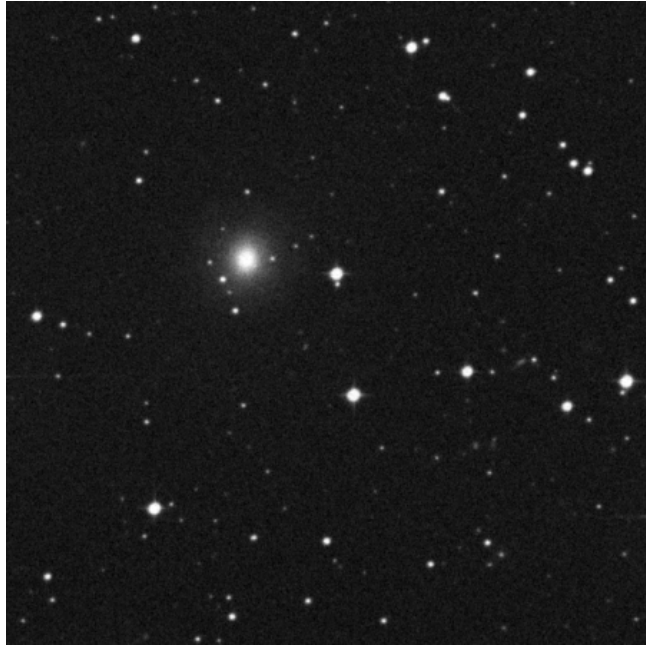
Figure 10: Light curves for off-axis jets as calculated with the complete integration and our simplified version. The agreement is surprisingly good, and justifies the usage of the simplified (and fast) calculation for our purposes.

We observe the agreement to be good on the paramter ranges of interest for our study case, and we conclude that our calculations are sufficient for our purposes. Note that full-fledged calculations, albeit available, would not suite our purposes as they are slow and not fit for parameter space exploration, as we will perform in the next section.

Band	Central frequency	Wavelength
Radio	3.0 GHz	10 cm
R	4.56×10^5 GHz	657 nm
X-ray	2.42×10^8 GHz	1.23 nm

Table 1: Frequencies of the EM bands of interest for our study

Time (days)	Flux (μJy)	Reference
16.42	18.7±6.3	[?]
17.39	15.1±3.9	–
18.33	14.5±3.7	–
22.36	22.5±3.4	–
24.26	25.6±2.9	–
31.22	34.0±3.6	[?]
46.26	44.0±4	–
54.27	48.±6	–
57.22	61.0±9	–
93.13	70.0±5.7	–
115.05	89.05±20	–
162.89	98.0±22.5	–
196.79	78.9±9	[?]
216.91	68.±21	[?]
256.76	55.±12	–

Table 2: 3 GHz fluxes considered for our study.

5 The afterglow of MMT170817: modelling and results

In this section, we will answer the question: What is the geometry and the dynamical structure of the matter emitting the observed afterglow?

This will lead us to decline various hypothese regarding the deceleration regime of the remnant and its geometry in order to find a coherent description of the phenomena.

5.1 Choice and reduction of multi-wavelength data

As described earlier, the afteglow emission was detected in X-ray, radio and visible bands respectively 9, 16 and ~ 150 d post-merger (when the kilonova had sufficiently dimmed in the case of the visible band). The homotetic sctructure of the light curves from different bands hints on the fact that all of these bands are in the same spectral regime. Indeed, taking the frequencies reported in table 8, and comparing to the scalings of ν_m and ν_c with the model parameters (reported in appendix B.2), we observe that in our case, all of the frequencies of interest are within the same range of the synchrotron spectrum. Namely, in the conditions of the remnant, we have $\nu_m \ll \nu_{\text{Radio,R,X}} \ll \nu_c$ at essentially all times.

In this domain of the spectrum, the flux scales as $F_\nu \propto \nu^{\frac{1-p}{2}}$. Thus, using the entire multi-wavelength set of photometry points, one can determine the value of p once and for all, and reduce the set of points to a single band (in our case the 3 GHz band) for the rest of the study. This is done in e.g. [?], and a value of $p = 2.22 \pm 0.1$ is found.

For now on, we will take $p = 2.2$, and use the radio 3 GHz points reported in table 2. Also, we will fix the value of ϵ_e to the fiducial value of 0.1 (see e.g. [?])

5.2 Can the afterglow come from a post-GRB relativistic jet?

The first appoach to solving the origin of the afterglow stems from the standard understanding of GRBs. According to this standard model (see e.g. [?], [?] sec. 5, [?]), sGRBs are produced by the dissipation of the kinetic energy of a relativistic jet into radiation by processes which are still to

elucidate. As described above, the later formation of a shock front by the jet and the plowing of interstellar material decelerates the jet and leads to the decollimation of the radiation emanating from the shocked material. If the decollimation and the emitted flux are such that an exterior observer enters the emission cone, than an afterglow from the relativistic jet is observed. Can this description explain the afterglow of MMT170817?

We calculate light curves produced in such a manner by a mono-kinetic jet of aperture θ_j, initial kinetic energy E_j[4] and uniform Lorentz factor Γ_0, penetrating an exterior medium of number density n and magnetic microphysical parameter ϵ_B, and observed from a angle of θ_{obs}.
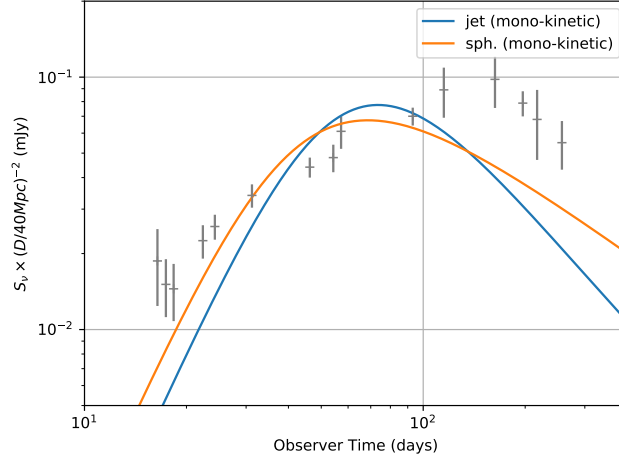
Figure 11: Best-fit light curve for the mono-kinetic jet afterglow model, and the monokinetic spherical shell model. None are an acceptable fit.

Figure 11 illustrates the monokinetic jet best-fit light curve to the radio points, obtained with a reduced χ^2 of $119/9 \sim 13$.

We observe that the characteristic $F(\nu, T) \propto T^3$ increase of jet afterglows does not fit the rather slow $F(\nu, T) \propto T^{0.79\pm015}$ (cf. infra) of the radio light curve. Furthermore, the smoothness of the jet afterglow peak constrasts with the strongly localized peak of the radio observations.

We may thus conclude that an acceptable fit to the radio data may not be found in the context of an afterglow produced by a jet-like outflow.

5.3 A quasi-spherical remnant

The jetted geometry for the afterglow emitter being ruled out, we now turn to the possibility that the shock front has a quasi-spherical geometry. In this case, the outflow of matter is almost spherical, and the corresponding shock front is a shell.

A mono-kinetic quasi-spherical remnant. For the same initial energies and Lorent factors, light curves from spherical and jet geometries will differ only after the jet break occurs for the jet model. Moreover, the relative weakness of the GRB hints to a likely small Lorentz factor for at least some of the matter ejected during the phenomena. Thus, we may predict that in our case of likely low Lorentz factor, spherical and jet geometry light curves of the monokinetic model will behave differently as of early times, the jet break occuring shortly for jet geometry cases.

Indeed, by adjusting only four parameters, n, ϵ_B, E_0 and Γ_0, a better fit is found for a monokinetic spherical ejecta model, as illustrated in figure 11. The corresponding reduced χ^2 is $72/11 \sim 6.5$. Nonetheless, this model also produces a steep increase, and we can conclude that the dynamics at hand in this model are not satisfactory.

A radially structured quasi-spherical remnant. We now turn to the radially structured remnant model. Recall this is a spherical outflow, but with components of various initial velocities, resulting in a continuous catching-up of the shock fromed by the fastest matter by slower matter when

---

[4]Notice that in this vision, the kinetic energy of the jet is the remainder of the jet's kinetic energy after dissipation in gamma radiation.

the shock decelerates. After the whole outflow has caught up to the shock, the dynamics are identical to those of a monokinetic outflow, but starting from the slowest velocity of the outflow.

In this case, the best fit light curve is found to lie close to the radio data, with $\chi^2 = 3.97/10 \sim 0.4$. The corresponding light curve is shown figure 12.
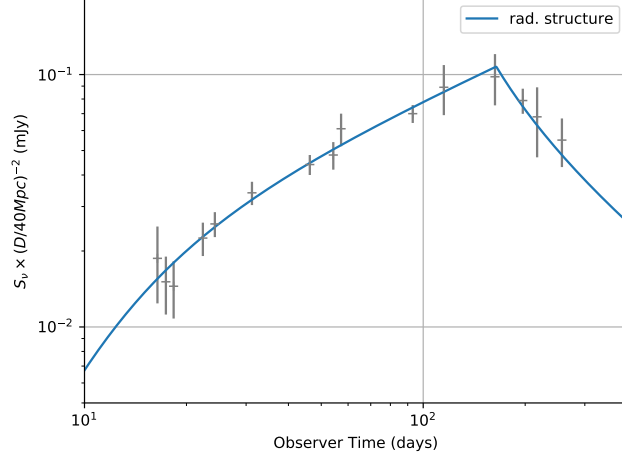

Figure 12: The best-fit light curve for the synchrotron emission model with a radially structured outflow.

The dynamical regime shift from catching-up to mono-kinetic shell allows for the sharp maximum of the light curve around 160 d post-merger. Remarkelbly, the increasing and the decreasing phase of the radio data are both correctly followed. We conclude that among the three models we have confronted, a radially structured quasi-spherical remnant reproduces the radio data with the most fidelity.

5.4   Conclusion

In conclusion, we have shown that in our model of synchrotron emission from shocked interstellar material as the origin of the afterglow of MMT170817, the most likely configuration is that the ejecta forming the shock has a quasi-spherical structure, and was ejected with a total kinetic energy of $\sim$ 6 $\times 10^{50}$ erg, with Lorentz factors in the range $\sim$ 2 $-$ 3, and it is expanding into a medium of number density $\sim$ 8 $\times$ 10^{-4} cm^{-3} and a magnetic microphysical parameter of $\sim$ 1 $\times$ 10^{-3}. Details on the actual best-fit parameters and their confidence intervals can be found in table 3.

6   Discussion around the results from the afterglow modelling

6.1   General discussion

Degeneracy of parameters and tightness of fit. Overall, there is an important degeneracy among the parameters of the radially-structured quasi-spherical model, as indicated by the low $\chi^2_{\rm red}$ of 0.4. Indeed, the cited best-fit values are indicative of the typical parameter to obtain the radio data, but small deviations from these values still produce acceptable light curves.

This is illustrated by studying the correlations between parameters. For the two external medium parameters n and ϵ_B, the χ^2 map projected on the (n, ϵ_B) plane around the best fit values is presented in figure 13. The correlation coefficient between the two variables is –0.6. Physically, a model is found tobe as close tothe data than the same model with a higher density and a lower magnetic parameter. This may be understood grossely by noticing that $B \propto \sqrt{(\epsilon_B n)}$, and thus for a same $\Gamma(r)$ (which depends on n), the emission will be equivalent by approximately conserving $\epsilon_B n$.

Similarly, we observe a strong anti-correlation between the dynamical parameter u_m and n, as shown figure 13. We observe that for u_m values smaller than best-fit, the global fitting error is invariant long lines of constant $n u_m^{-\beta}$, where $\beta \sim 5 = \alpha$. Coming back to the dynamical equation $(V(r) = 4\pi r^3/3)$:

Parameter	Best-fit values (1σ confidence interval)
$\bar{n}$	$(8.1 \pm 1.5) \times 10^{-4} \mathrm{cm}^{-3}$
$\bar{\epsilon_B}$	$(8.1 \pm 1.5) \times 10^{-4}$
$\bar{E_0}$	$(5.61 \pm 0.6) \times 10^{50} \mathrm{erg}$
$\bar{u_m}$	1.5 ± 0.02
$\bar{u_M}$	$3.19 \pm 1.$

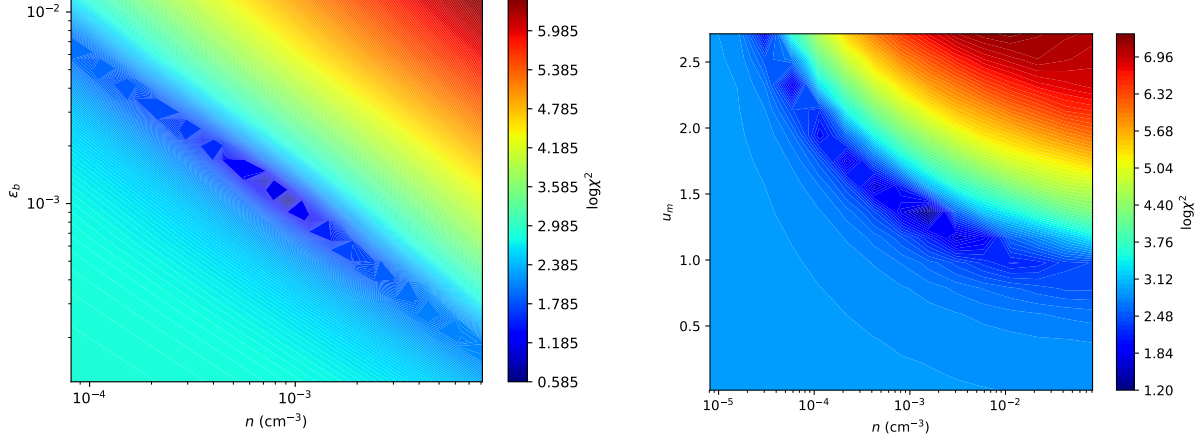Table 3: Best-fit parameter values for the quasi-spherical shock with radial velocity structure.

Figure 13: Projected likely-hood map on the fitting of the external parameters n and ϵ_B (left) and n and u_m (right) in the radially structured ejecta model.

$$V(r)c^2 n(u_m^{-\alpha} - u_M^{-\alpha}) = E_0(u^{-\alpha} - u_M^{-\alpha})$$

It appears that if $u_m^{-\alpha} \gg u_M^{-\alpha}$, which is the case for our $\alpha = 5$ and $u_m < \bar{u_m} \sim 1.5$, then the dynamic equation simplifies to:

$$V(r)c^2 n u_m^{-\alpha} = E_0(u^{-\alpha} - u_M^{-\alpha})$$

by which the dynamics are solely determined by the product $n u_m^{-\alpha}$ as suggested by the anti-correlation we observe.

Also, we deduce from table 3 that the best-constrained parameter is u_m. As explained previously, u_m determines the momentwhen the dynamics switch from the catching-up phase to the monokinetic regime, consistently producing a sharp break in the dynamical behavior and thus in the light-curve. As the radio data point out, the flux features a sharp light curve maximum, and it is thus understood that the time of dynamical regime shift must be well determined and thus u_m tightly constrained.

What *is* the ejected matter? As we have seen, the aterglow does not likely originate from a post-GRB relativistic jet. It is more likely in a quasi-spherical shape, and was ejected with inhomogeneous velocities. This unfortunately does not inform us on the nature of this ejected matter, i.e. its composition, the process during which, when and from where it was ejected.

It may have been ejected by the friction of the two neutron stars upon coalescence, and later have formed an accretion disk around the final central object and finally been blown away by a thermal neutrino wind, producing the kilonova radiation in the process. It may also be have been emitted by an intermediate central compact object during its relaxation to its final structure as a black hole or neutron star.

It is likely that the answers to these interrogations lie in the signatures of earlier phases of the phenomenon, such as the kilonova. In particular, as illustrated in figure 14 and table 3, the maximum ejection velocity u_M is the most poorly constrained parameter of the radially-structured quasi-spherical model, for lack of early radio points.
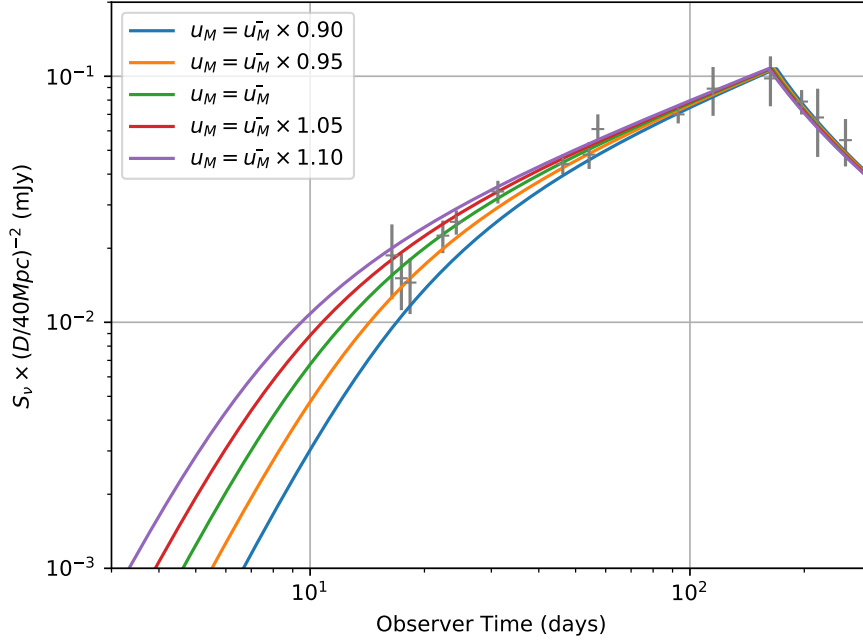
Figure 14: Radially structured model light curves with varying u_M and best-fit values for all other paramters. u_M would be better constrained with earlier flux measurements.

Measuring radio fluxes at earlier times would allow better constraints on u_M and thus a better understanding of the ejection conditions, and therefore of the nature of the ejected matter.

Furthermore, it is possible that the matter currently plowing the exterior medium was not ejected simultaneously. Indeed, in the so-called *cocoon model* ([**?**, **?**],), a relativistic jet impacts some previously ejected matter, depositing supplementary kinetic energy, and thereby *choking* the GRB. This results in no classical jet-produced GRB, but rather in a higher-energy quasi-spherical ejecta producing a weak GRB and eventually a quasi-spherical remnant and shock. Nonetheless, these models concern the origin of the shock-forming matter while our calculations are only concerned with the geometry of this matter and it's final velocity distribution.

6.2 The external medium

The best-fit density parameter $\sim 10^{-3}$ cm^{-3} value is broadly consistent with typical values inside gas-rarified early-type galaxies such as NGC4993 ([**?**]).

More precisely, according to recent measurements of HI 21-cm fluxes in the host galaxy of MMT170817 ([**?**]), an upper limit on the galaxtic density of atomic hydrogen is found to be $n_{\mathrm{HI}} < 4 \times 10^{-2}$ cm^{-3}. If we suppose (as we have already done in our calculations) that the local medium is composed essentially of hydrogen, this upper limit is consistent with our model's predictions.

Similarly, with a star formation rate measured to $\sim 10^{-2}$ $M_{\odot}$/yr ([**?**]) and using the Kennicut-Schmidt law [**?**], the average density of HI in NGC4993 is estimated to $\sim 4 \times 10^{-3}$ cm^{-3} ([**?**]), assuming the HI content to extend out to ~ 18 kpc from the center of NGC4993. This is roughly a factor of 2 above our prediction. As illustrated in figure 16, the projected position of the coalescence site is well inside the buldge of NGC4993. The angular distance from the merger site to the center of the galaxy is $\sim 10,6''$, equivalent to 2.12 kpc at 40 Mpc.

Consequently, the discrepancy in estimates of local density can be explained either by the fact that the merger site is in fact in a peripheral region of the galaxy, where the density is lower than the average, or on the contrary that the merger site is well inside the galaxy as suggested by the projected position, but the gas and dust content of NGC4993 does not follow an ordinary radially-decreasing profile. This last possibility is further supported by the presence of shell structures in NGC4993 as shown by [**?**], indicating a recent galactic merger event implicating the host galaxy, therefore explaining a non-trivial distribution of gas in NGC4993 and finally the possibility for lower-than-average densities even in central regions of the galaxy.

How likely is the merger site to be in the central region of NGC4993? Supposing that the merger site was drawn from a uniform distribution of points in the galaxy of radius R_G, the observation of the projected radial distance at $R_{\mathrm{proj}} = 2.12$ kpc implies a posterior probability distribution for the actual radial distance R from the galacitc center to the merger locus. This distribution is illustrated in fig 15, where we have followed [?] in taking $R_G = 9$ kpc (stellar extent).
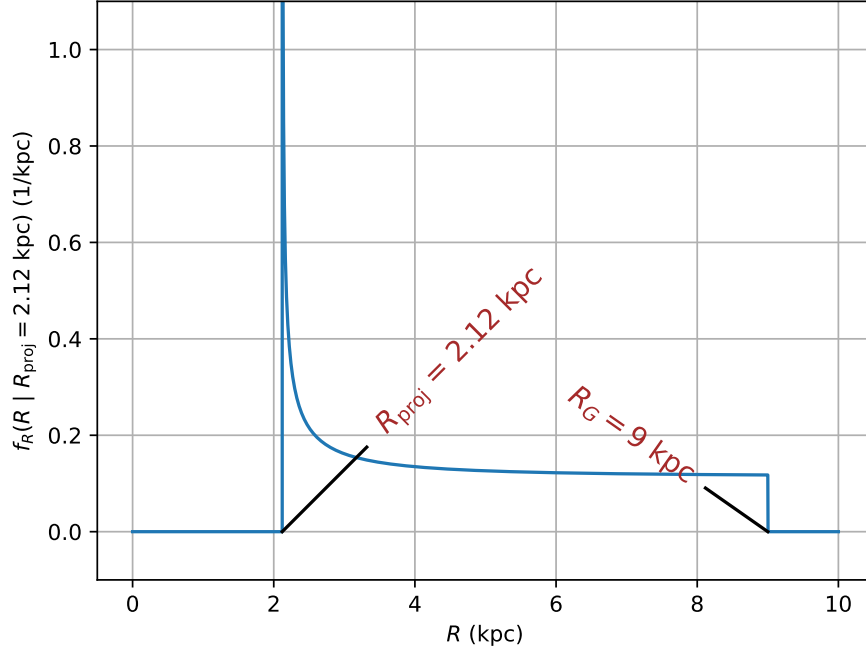

Figure 15: Probability density distribution for the radial distance of the merger locus to the galactic center, knowing the projected radial distance to be 2.12 kpc, and supposing the merger point drawn at random in the 9 kpc-radius galaxy.

We observe that the distribution is highly peaked around the projected distance, and nearly uniform in the rest of the density space. It is thus likely that the merger site is really in the center of the galaxy, and if it is not then no further conclusion can be drawn.
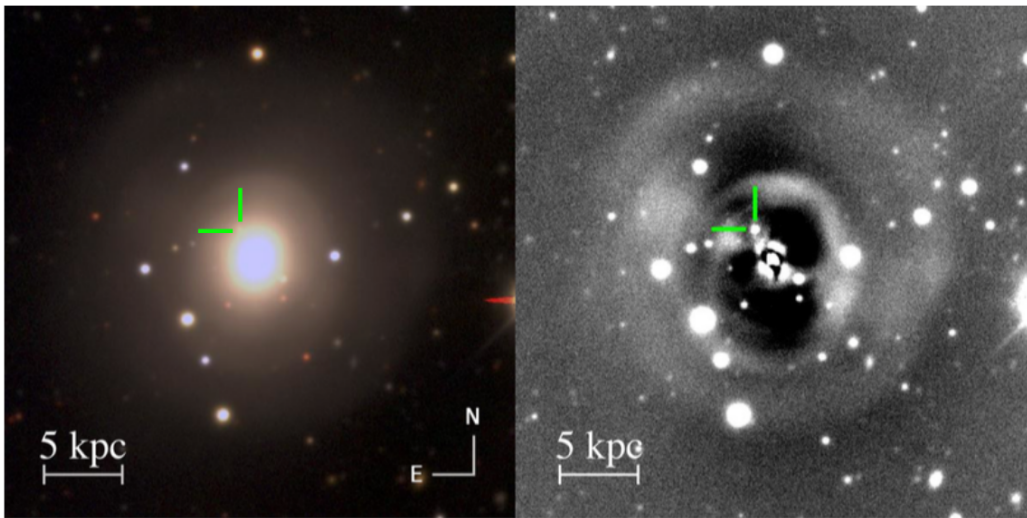
Figure 16: Localisation of the merger site as projected on the sky plane in NGC4993 ([?]).

24
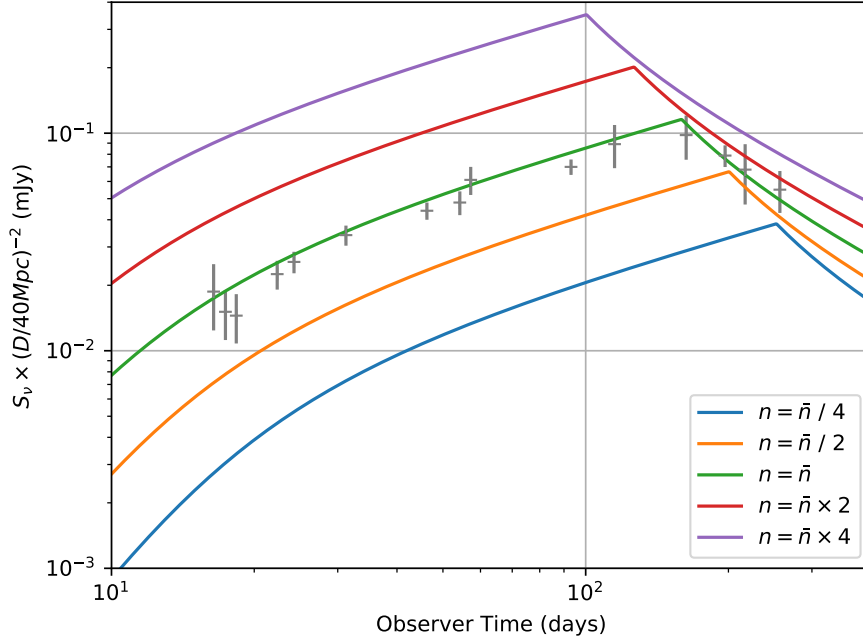
Figure 17: Radially structured model light curves with varying exterior density n and best-fit values for other parameters.

6.3 What of the standard relativistic jet?

We found in the previous section that the radio observations could not be understood as the afterglow emission from a jet-structured outflow. Nonetheless, this jet is predicted by standard model of short GRBs. The non-observation of a jet-like afterglow emission therefore constrains the characteristics of any relativistic jet which would have occured and produced the GRB. Furthermore, if we require coherence of these constrained jets with sGRB observations and models, then constrains on the characteristics of the exterior medium are found.

What can we learn of the eventual relativistic jet from its non-observation until now?

What can we infer on the external medium by confronting these jets with sGRB observations?

Hiding the jet afterglow. How may we translate the non-observation of the jet in terms of jet afterglow time of peak and peak flux?

A first approach is to require that the jet-induced afterglow peak flux F_j^p be weaker than the observed radio flux *at the time of the jet afterglow peak* t_j^p. This of course is a weaker constrain than to require that the jet afterglow flux be *weaker than the observed fluxes at all times*. We call this the *jet hiding* condition. A mathematical formulation is:

$$F_j^p < F^{\text{obs}}(\nu, t_j^p)$$

Figure 18 illustrates our method to translate this into conditions in parameter space. Suppose that F_j^p and t_j^p are given in terms of a power-law on the parameters E_j, n, etc. which we will note p_1, p_2 for now. That is:

$$F_j^p = F_0 p_1^{\alpha_1} p_2^{\alpha_2} \dots$$

and

$$t_j^p = t_0 p_1^{\beta_1} p_2^{\beta_2} \dots$$

Then, suppose that the radio light curve be given by a power law as well, that is:

$$F^{\text{obs}}(\nu, t_{\text{obs}}) = F^{\text{obs}}{}_0 t_{\text{obs}}{}^\gamma$$

25

Now, the hiding condition is thus rewritten:

$$F_0 p_1^{\alpha_1} p_2^{\alpha_2} \cdots < F^{\text{obs}}_0 \left(t_0 p_1^{\beta_1} p_2^{\beta_2} \cdots \right)^{\gamma}$$

Which in fact results in a *sublinear condition* on the parameters for the jet to be hidden:

$$(\alpha_1 - \gamma\beta_1) \log p_1 + (\alpha_2 - \gamma\beta_2) \log p_2 + \cdots < \log \left(\frac{F^{\text{obs}} t_0^{\gamma}}{F_0} \right)$$

The gemoetrical interpretation of this is simple: the indices α_i and β_i are just the coordinates of the vectors by which is dispaced themaximum of the jet afterglow if the parameters are multiplied by 10. The hiding condition is then simply the condition on any linear combination of these vectors so that the jet remain hidden when displacing the maximum, hence changing the underlying parameters.
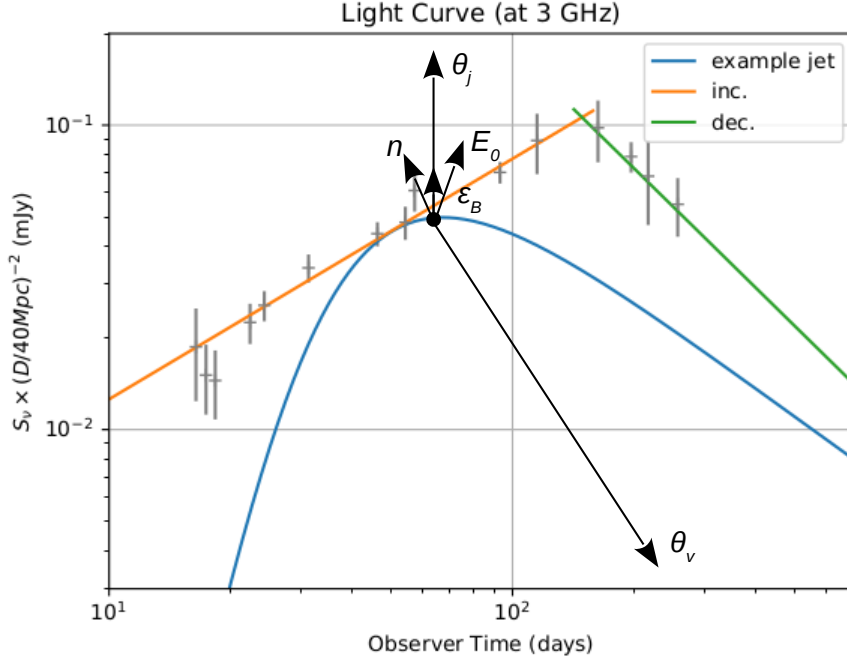
Figure 18: Illustration of the method used to obtain constraints on the relativistic jet. Changing the jet parameters will displace the maximum of the jet afterglow light curve along the vectors showed here. Requiring that the maximum be always weaker than the radio points amounts to sublinear conditions on the jet parameters.

After a thorough exploration of the parameter space, we infer that the peak time and peak flux of a jet-induced afterglow consistently scale like the following with the jet parameters and exterior medium parameters[5]:

$$F_j^p = 121 \ \mu\text{Jy} \left(\frac{E_j}{10^{52} \ \text{erg}} \right) \left(\frac{n}{10^{-3} \ \text{cm}^{-3}} \right)^{4/5} \left(\frac{\epsilon_B}{10^{-3}} \right)^{4/5} \left(\frac{\theta_{\text{obs}}}{0.25 \ \text{rd}} \right)^{-4.3} \left(\frac{\theta_j}{0.1 \ \text{rd}} \right)^{2}$$

$$t_j^p = 37.4 \ \text{d} \left(\frac{E_j}{10^{52} \ \text{erg}} \right)^{1/3} \left(\frac{n}{10^{-3} \ \text{cm}^{-3}} \right)^{-1/3} \left(\frac{\theta_{\text{obs}}}{0.25 \ \text{rd}} \right)^{8/3}$$

We model the observed light curve as a broken power-law as illustrated in figure 18. We obtain the following:

$$F^{\text{obs}}(3 \ \text{GHz}) = \begin{cases} (77.6 \pm 12.1) \ \mu\text{Jy} \left(\frac{t_{\text{obs}}}{100 \ \text{d}} \right)^{0.791 \pm 0.152} & \text{if } t_{\text{obs}} < 163 \ \text{d} \\ (45.4 \pm 41.7) \ \mu\text{Jy} \left(\frac{t_{\text{obs}}}{300 \ \text{d}} \right)^{-1.29 \pm 1.56} & \text{if } 163 \ \text{d} < t_{\text{obs}} \end{cases}$$

---

[5]The initial Lorentz factor of the ejecta Γ_0 is not relevant here because as detailed in the previous section, the dynamics in the relativistic deceleration phase (during which the peak occurs) no longer depend on Γ_0

In conclusion, a set of jet parameters and exterior medium parameters will give rise to a hidden jet if:

$$\begin{cases} F_j^p < 77.6 \ \mu\text{Jy} \left(\frac{t_j^p}{100 \ \text{d}} \right)^{0.791} \\ \text{and} \\ F_j^p < 45.4 \ \mu\text{Jy} \left(\frac{t_j^p}{300 \ \text{d}} \right)^{-1.29} \end{cases}$$

taking the central values on the power-law fitting of the light curve.

In turn, this translates in parameter space to[6]:

$$\begin{cases} 0.736 x_{E_j} + 1.06 x_n + x_{\epsilon_B} - 5.35 x_{\theta_{\text{obs}}} + 2 x_{\theta_j} < -0.531 \\ \text{and} \\ 1.43 x_{E_j} + 0.37 x_n + x_{\epsilon_B} - 0.49 x_{\theta_{\text{obs}}} + 2 x_{\theta_j} < 0.74 \end{cases}$$

These are two sublinear conditions in the 5-dimensional space of jet and medium parameters which are implied by the non-observation of a jet-induced afterglow.

We will now further discuss the eventuality of a relativistic jet and constrain the external medium by specifying some values for some of the parameters in these two sublinear conditions. These values will come either from our previous results (on n and ϵ_B, coming from the fitting to the radially structured remnant light curve), or results from the gravitational wave community (on θ_{obs} mainly) or previous observations and models for GRBs (on E_j).

Further constraints on the external medium. We will now use these set of conditions to better constrain the external parameters n and ϵ_B.

In order to obtain conditions of n and ϵ_B only, we must estimate values for E_j, θ_{obs} and θ_j. Then, the two sublinear constrains which we have derived from the non-pbservation of a jet-like geometry will concern only the exterior medium, through n and ϵ_B.

Which estimate for E_j? The fluence of GRB170817A is $(2.08 \pm 0.2) \times 10^{-7}$ erg cm^{-2}, and the isotropic equivalent dissipated energy is E_γ^{iso} ... . In the standard vision where the GRB was produced by a relativistic jet, this is the total kinetic energy of the jet which was dissipated in gamma rays. The kinetic energy of the jet producing the afterglow is thus the remainder of this kinetic energy. By denoting E_0^K the initial kinetic energyof the jet, we thus have:

$$E_0^K = E_\gamma^{\text{iso}} + E_j$$

E_j still designating the kinetic energy available for the afterglow if the jet (and which is considered by our model). We now introduce the *gamma efficiency* parameter f_γ, which quantifies the efficiency of the dissipation of kinetic energy into gamma rays in the GRB phase, i.e. $f_\gamma = E_\gamma^{\text{iso}}/E_0^K$. The efficiencies based on kinetic energy measurements vary from some % to many tens of % ([**?**, **?**]). Using this definition, it follows that:

$$E_j = \frac{1 - f_\gamma}{f_\gamma} E_\gamma^{\text{iso}}$$

As for the viewing angle, the gravitational wave data indicates an upper limit $\theta_{\text{obs}} < \theta_{\text{obs}}^{GW} = 28 \deg$. We will thus consider various viewing angles below this limit.

For various values of f_γ, for $\theta_{\text{obs}} = \theta_{\text{obs}}^{GW}$ and $\theta_{\text{obs}}^{GW}/2$, we plot the exclusion diagram in the (n, ϵ_B) plane in figure 19. We have superimposed the error map from the radially structured model (figure 13) for reference.

---

[6]We introduce the notations $x_{E_j} = \log \left(\frac{E_j}{10^{52} \ \text{erg}} \right)$, $x_n = \log \left(\frac{n}{10^{-3} \ \text{cm}^{-3}} \right)$, $x_{\epsilon_B} = \log \left(\frac{\epsilon_B}{10^{-3}} \right)$, $x_{\theta_{\text{obs}}} = \log \left(\frac{\theta_{\text{obs}}}{0.25 \ \text{rd}} \right)$, $x_{\theta_j} = \log \left(\frac{\theta_j}{0.1 \ \text{rd}} \right)$.
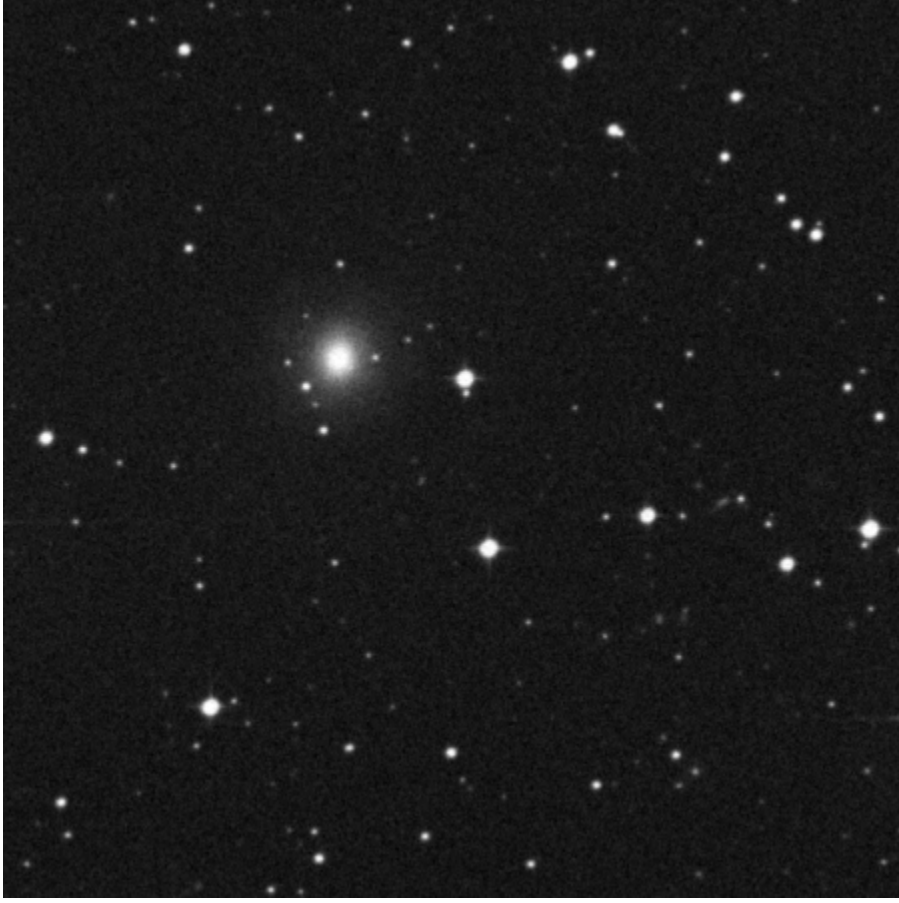
Figure 19: Superposition of the error map on the fitting of n and $epsilon_B$ to the quasi-spherical radially structured remnant and of the sublinear constraints on these parameters obtained from the hiding of the jet.

Discussion on the intrinsic characteristics of the jet. We now turn to constraining the instrinsic characteristics of the jet. Again, the two sublinear conditions that we have established imply all 5 parameters of a jet afterglow. If we seek constrains on the jet parameters only (E_j, θ_j), independently of exterior factors, then we must fix the three parameters n, ϵ_B and θ_{obs}. Lukily, we have estimates for n, ϵ_B as provided by our fitting to the radially structured model which we can take. Also, we can as above vary θ_{obs} in the range indicated by the gravitaional wave data from GW170817.

These constraints in the (E_j, θ_j) plane are illustrated in figure 20. The non-shaded region corresponds to possible hidden jets given the likely values of n and ϵ_B provided by the fitting of the afterglow with a spherical radially structured remnant.
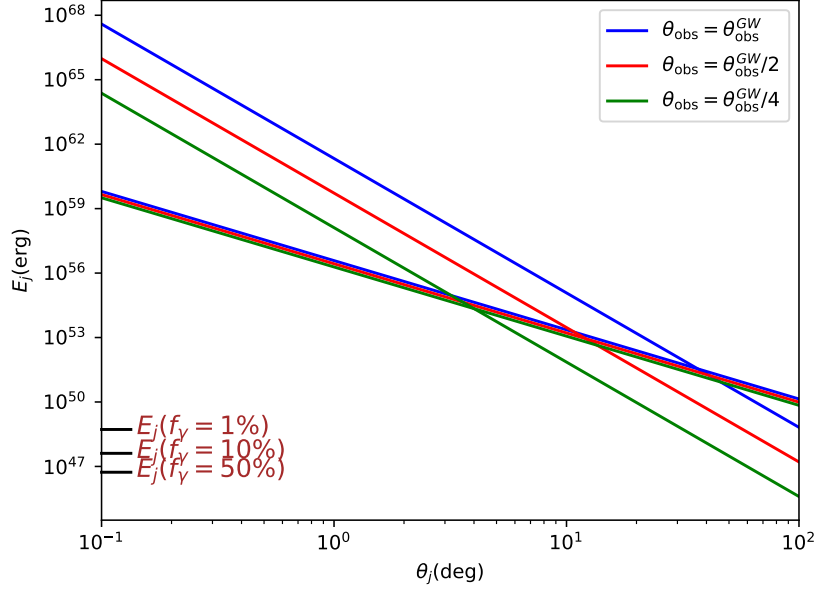
Figure 20: Constraints on the intrinsic parameters of the relativistic jet, as visualized in the (θ_j, E_j) plane for various values of $\theta_{\rm obs}$ below $\theta_{\rm obs}^{\rm max} = 28\,{\rm deg}$.

What would we have seen as on-axis observers of these hidden jets?
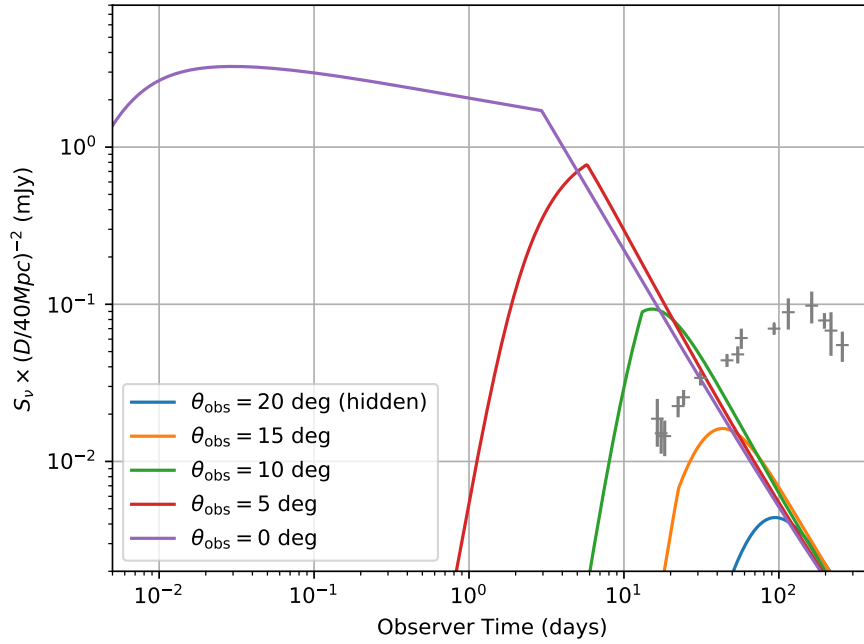
Figure 21: Afterglow light curves of on-axis observers for a hidden jet.

Jet-induced bumps. Of course, our hiding condition on the maximum of the jet afterglow does not fully characterize the non-observation of a jet afterglow. Indeed, if the jet afterglow decays slower than the $t^{-1.3}$ of the radio data, than the jet can create bumps, as illustrated in figure 22. Thus, the parameter space which we have excluded here is in fact too loose of a constraint on the jet. In the data of MMT170817 a bump has yet to be found.
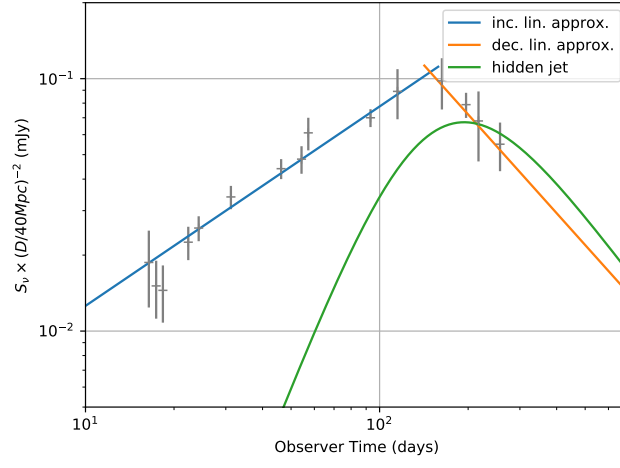
Figure 22: A jet afterglow which complies to our hiding condition (the maximum is weaker than the data at the time of maximum), yet the afterglow is clearly apparent.

Part III

Perspectives on the study of binary neutron star mergers

MMT170817 is the first neutron star merger event observed, and is was so with the capabilities of multi-messenger astronomy. As we have shown, it is a peculiar event in several respects, and though its afterglow informs us on some aspects of the dynamics which occured in the event an on the possibility that a jet was produced, many questions remain. What is to come in the study of binary neutron star mergers?

7 Observation perspectives

7.1 Future rates of events and counterparts

A single event was observed until now. As we have shown, the overall observations are the product of various factors, some intrinsic to the event – the ejection energy, velocity, mass, etc. –, some intrinsic to the event locus – external medium density and microphysics parameters –, and finally some extrinsic – viewing angle, distance. We may ask what is the diversity of these events, and can the external diveristy be *factored out* in order to obtain a description of the merger event itself?

Clearly, any result in this sense will come from a large number of observations. We will review here some estimates for future rates of mergers and electromagnetic counterparts.

Gravitational wave signals. The detection of GW170817 allowsto infer to BNS merger rate in the local Universe to be 1540^{+3200}_{-1220} Gpc^{-3}yr^{-1} [**?**]. The joint three-detector observation run named O3 should start mid 2019, as announced by the LSC-Virgo Collaboration ([**?**]). It should last one year and the BNS range[7] is predicted to ~ 150 Mpc. Taking a three-instrument duty cycle (the fraction of observation time when all three instruments are online) of 45% ([**?**]), this results in 10^{+20}_{-8} BNS merger GW detections during the O3 run. As we have already described, the detection range is determined by the largest range of the three instruments, while the ranges of the others impact thelocalization capabilities. At the design sensitivity of 190 Mpc, predicted for 2021, this is 20^{+40}_{-16} per cummulated year of observing run.

Gravitational waves with kilonova. What are the chances to detect a kilonova associated to a GW signal? The first remark is that kilonovae emissions are likely isotropic, as the typical scenario suggests. Thus, contrarely to GRBs, the only limiting factor to kilonovae detection is the distance to the source, and not the observing angle.

The second remark is that in the case of binary neutron star mergers, nuclear processes are likely to consistently occur (and drive a kilonovae emission) in the sequel of merger events. These will happen either in dynamical ejecta in the case of collisions, in the tidal ejecta in case of a tidal disruption event (for highly asymmetrical binaries) or in the wind produced by some accretion disk formed of these ejectas. Thus, a kilonova emission (possibly with various components due to different ejecta of varying opacities and masses) should be associated to any BNS merger event.

Finally, it seems that the only parameters relevant to determining the composition and the dynamics of the kilonova are the initial masses and spins of the neutron stars. Indeed, the final orbits of the binary are fully determined by these, and thus the mass and velocity of the ejecta is determined solely by these, and its composition and opacity are determinded solely by the (unique albeit unknown) equation of state of nuclear matteer. Therefore, we predict little variability in the kilonovae of binary neutron star mergers. If kilonovae are indeed standard candles, and their absolute magnitudes are all of –16 like AT 2017gfo, then kilonovae can be detected out to ~ 250 Mpc, assuming a photometric quality maximum-detectable magnitude of 21.

Thus, the kilonova range is larger than the BNS GW range, even for dimmer kilonovae. Given that GW are systematically the trigger for the detetion of merger events, ad that they are the only

---

[7]The sky-position averaged distance at which the GW from a merger of a $1.4M_\odot$-$1.4M_\odot$ binary neutron star can be detected by a detector. It takes into account the instrumental sensitivity variations dueto the orientation of the interferometer with respect to the source. Another frequently cited figure is the BNS *horizon*, which is the distance to which an optimally oriented such binary merger can be detected. The range is 2.26 times lower than the horizon.

source of a resrictive-enough error box for the search of electromagnetic couterparts, we conclude that the kilonova rate equals the BNS merger GW rate.

Afterglow detections. Contrarely to kilonovae, the afterglow emission depends on many parameters, as we have detailed in this work. There will likely be a large diversity in afterglow emissions. Nonetheless, once a transient optical source is detected in the error box provided by the GW signal, then the source is pinpointed to sub-arcsecond precision, and an afterglow can be either detected, or constrained by upper limits. Thus the rate of astronomically interesting study cases concerning BNS merger afterglows is the same as the kilonova rate, which in turn amounts to the GW detection rate.

Coincident GRBs.

In conclusion, we can say that apart from the GRB counterpart, for which it is difficult to make rate predictions, the rates of both BNS merger-induced kilonova detections and remnant detections or upper limits is essentially the same as the rate of BNS merger GW detections. The latter is conditionned by the population of binary neutron systems in the local Universe, and by the sensitivity of the gravitational interferometers. A current prediction is 10^{+20}_{-8} detections for the one-year O3 run to come.

7.2   Insights on other astronomical observables

In this work we were concerned with the afterglow light curve of MMT170817. As we have seen, it allows us to infer much information on the global phenomenon of neutron star mergers: from the exterior medium to the structure of the ejectas and the possibilities for a relativistic jet.

What may other astronomical observables teach us on this phenomenon?

Polarization of the afterglow emission. The polarization of the afterglow emission can be calculated similarly to the afterglow flux. Synchrotron emission is naturally polarized, and the overall polarization of the afterglow will depend on geometrical hypotheses concerning the shock itself (jet-like, spherical) and the magnetic field. For example, spherical symmetry arguments allow to conclude that the linear polarization of the emission from a spherical shock front vanishes. On the other hand, if the remnant is jetted (in a cone shape), then the polarization can be important, if the system is seen off-axis. Also, according to whether the magnetic field is contained in the shock plane or has a non-zero longitudinal component, the linear polarization of the emission will change.

We notice here that is the ejecta is composed of various ejectas with different geometries (such as a jet with a quasi-spherical outflow), it is possible that a jetted ejecta may not be visible in photmetry, due to its small flux compared to the quasi-spherical outflow, but readily discernable by the polarization that it induces in the overall flux. Certain authers such as [?] predict linear polarizations as large as 60% in some models for MMT170817 where a jetted ejecta formed along with a quasi-spherical ejecta.

At these fluxes ($\sim 10~\mu\mathrm{Jy}$), the polarization of the emission is readily measured, and can be a supplementary means of sounding the presence of a jet through the afterglow emission.

Radio imaging of the remnant. Given the relative proximity of the locus of MMT170817 and the typical velocities of the remnant's expansion, the angular diameter of the remnant can be estimated to be $\sim 0.1 - 10$ mas at the time of peak flux [?]. This angular resolution is within the capabilities of global very long base radio interferometry networks. Then, the actual shape of the remnant would be accessible, and the geometry and dynamics of the outlfow could be assessed in large detail.

7.3   Insight on future modelization

Reverse shock.

8   Open questions

What GRBs can be produced by the hidden jets? s this event a particular case of a standard GRB or must a new understanding of GRB specifically neutron star mergers be found?

What is the nature of the resulting compact object?

What is the intrinsic diversity of the merger phenomenon?

Appendix A: Terminology

The novelty of the observing of binary neutron star mergers and the diversity of models describing this phenomenon render the full agreement of the high-energy community on some terms difficult. That is why a concise bilingual glossary is found here.

Remnant (*Reste*). All of the matter in the vicinity of the merger locus and which either was a part of the neutron stars or is being swept up by the latter.

Quasi-spherical remnant ().

Appendix B: Details on the physics of afterglows

B.1: Dissipation of kinetic energy in realtivistic shocks

We will derive here the equation for the conservation of energy in the collision of two masses at relativistic speeds with dissipation of kinetic enrgy to internal energy. For this consider a mass M in relativistic motion at a Lorentz factor Γ impacting a small mass m at rest. What will be the final energy of the small mass?

Let Γ' denote the Lorentz factor of the joint mass $M + m$ after the collision. We suppose that some dissipation of kinetic energy has occured during the collision, and that the small mass has a rest energy $\gamma_i m c^2$ after the interaction.

In an external rest frame, the conservation of energy and momentum thus reads:

$$\Gamma M c^2 + m c^2 = \Gamma' M c^2 + \Gamma' \gamma_i m \tag{19}$$

$$\Gamma \beta M + 0 = \Gamma' \beta' \gamma_i m \tag{20}$$

It follows the post-collision speed, which is rightly decelerated:

$$\beta' = \beta \frac{\Gamma M}{\Gamma M + m} \tag{21}$$

Supposing a high initial Lorentz factor and a small m/M mass ratio, we have $\beta \sim 1 - 1/2\Gamma^2$ and $\frac{\Gamma M}{\Gamma M + m} \sim 1 - m/\Gamma M$. Thus rearanging 21 leads after some algebra to:

$$\Gamma'^2 = \frac{\Gamma^2}{1 + 2\Gamma \frac{m}{M}} \tag{22}$$

and then:

$$\frac{\Gamma}{\Gamma'} = 1 + \Gamma \frac{m}{M} \tag{23}$$

Thus, we conclude that:

$$\gamma_i = \frac{\Gamma M + m - \Gamma' M}{\Gamma' m} \tag{24}$$

$$\sim \left(\frac{\Gamma}{\Gamma'} - 1 \right) \frac{M}{m} \tag{25}$$

$$\sim \Gamma' \tag{26}$$

And thus the overall energy conservation writes:

$$\Gamma M + m = \Gamma' M + \Gamma'^2 m \tag{27}$$

or in the continuous form after sweeping a mass $m(r)$ of exterior material:

$$\Gamma_0 M + m(r) = \Gamma(r) M + \Gamma(r)^2 m(r)$$

B.2: Scalings of ν_m and ν_c

The synchrotron characteristic frequencies are found to scale as the following with the model parameters in the various dynamical phases of the afterglow. They are normalized to the parameters' values which we infer in the text. These scalings allow to compare the observation bands (X-ray, optical and radio) to the typical spectral regime shift frequencies, and thus to conclude that all the observation bands are within the same spectral regime.

Coasting phase:

$$\nu_m = 10.2 \text{ GHz} \left(\frac{\Gamma_0}{10}\right)^4 \left(\frac{n}{10^{-3} \text{ cm}^{-3}}\right)^{1/2} \left(\frac{\epsilon_B}{10^{-3}}\right)^{1/2} \left(\frac{\epsilon_e}{0.1}\right)^2 \left(\frac{\frac{p-2}{p-1}}{0.167}\right)^2$$

$$\nu_c = 9.56 \times 10^8 \text{ GHz} \left(\frac{\Gamma_0}{10}\right)^{-4} \left(\frac{n}{10^{-3} \text{ cm}^{-3}}\right)^{-3/2} \left(\frac{\epsilon_B}{10^{-3}}\right)^{-3/2} \left(\frac{t_{\text{obs}}}{10 \text{ d}}\right)^{-2}$$

Deceleraton phase:

$$\nu_m = 1.78 \times 10^{-4} \text{ Hz} \left(\frac{E_0}{10^{51} \text{ erg}}\right)^{1/2} \left(\frac{\epsilon_B}{10^{-3}}\right)^{1/2} \left(\frac{\epsilon_e}{0.1}\right)^2 \left(\frac{\frac{p-2}{p-1}}{0.167}\right)^2 \left(\frac{t_{\text{obs}}}{100 \text{ d}}\right)^{-3/2}$$

$$\nu_c = 4.38 \times 10^{21} \text{ GHz} \left(\frac{E_0}{10^{51} \text{ erg}}\right)^{-1/2} \left(\frac{n}{10^{-3} \text{ cm}^{-3}}\right)^{-1} \left(\frac{\epsilon_B}{10^{-3}}\right)^{-3/2} \left(\frac{t_{\text{obs}}}{100 \text{ d}}\right)^{-1/2}$$

Newtonian phase:

$$\nu_m = 1.46 \times 10^{-10} \text{ Hz} \left(\frac{E_0}{10^{51} \text{ erg}}\right) \left(\frac{n}{10^{-3} \text{ cm}^{-3}}\right)^{-1/2} \left(\frac{\epsilon_B}{10^{-3}}\right)^{1/2} \left(\frac{\epsilon_e}{0.1}\right)^2 \left(\frac{\frac{p-2}{p-1}}{0.167}\right)^2 \left(\frac{t_{\text{obs}}}{10^5 \text{ d}}\right)^{-1/2}$$

$$\nu_c = 1.11 \times 10^{40} \text{ GHz} \left(\frac{E_0}{10^{51} \text{ erg}}\right)^{-3/5} \left(\frac{n}{10^{-3} \text{ cm}^{-3}}\right)^{-9/10} \left(\frac{\epsilon_B}{10^{-3}}\right)^{-3/2} \left(\frac{t_{\text{obs}}}{10^5 \text{ d}}\right)^{-1/5}$$

B.3: Short discussion on the origin of magnetic fields in astrophysical shocks

List of Figures

List of Tables

References

hi